J. Webster (ed.), *Wiley Encyclopedia of Electrical and Electronics Engineering*

PLANAR DIELECTRIC LEAKY-WAVE ANTENNAS

Introduction

Millimeter-wave systems have found a continually growing spectrum of applications. Whereas previous applications usually had a military background (1) present and future developments will largely focus on millimeter-wave communications (2) and consumer-oriented applications such as automobile sensors for collision-avoidance radar (3). Advantages of millimeter-wave systems compared to microwave systems are higher directivity and more usable bandwidth (4). Compared to optical systems, millimeter-wave systems are much less susceptible to atmospheric influences.

The antenna itself is always the interface between a communication or sensor system and the environment. Highly directive antennas reduce transmitter power due to their narrower beams, which also implies reduction of interference from other sources. This implies increased signal-to-noise ratio for communication systems and increased sensitivity for sensor systems. A good overview of millimeter-wave antennas can be found in Ref. 5

One very attractive class of antennas for millimeter-wave applications is the class of leaky-wave antennas (6). Leaky-wave antennas have the advantage of being able to produce highly directive beams with a relatively simple structure. Leaky-wave antennas generally consist of a structure that supports the propagation of one or more leaky waves, which are waves that radiate (leak power) as they propagate. Because of the radiation, the leaky wave has a complex propagation constant of the form $\beta - j\alpha$, where β is the phase constant and α is the leakage (attenuation) constant. The structure is designed so that the power leakage occurs at a fixed angle into space, determined by β, resulting in a radiation pattern that has a narrow beam centered at this angle. The structural parameters also determine the leakage constant of the leaky wave, which determines the beam width of the radiation pattern. A smaller leakage constant results in a larger effective radiating aperture (unless restricted by the physical size of the antenna aperture), which in turn results in a narrower beam and hence higher directivity. Because leaky-wave antennas achieve a radiating aperture distribution by virtue of a propagating wave instead of a power distribution network, the associated feed losses are avoided, resulting in improved efficiency at millimeter-wave frequencies.

Two general classes of leaky-wave antenna exist: fast wave and slow wave. In a fast-wave antenna, the leaky mode is a fast wave, meaning that the phase velocity is greater than that of light in free space ($\beta < k_0$. The leaky wave thus radiates directly into space at an angle determined by the phase constant β. The guiding structure that supports the leaky wave may be a uniform structure or a periodic structure. An example of this type of antenna is a rectangular waveguide with a longitudinal slot (uniform structure) or a periodic array of slots (periodic structure). Another example is the microstrip-line antenna, in which the leaky wave is a higher-order mode on the microstrip line (7).

In a slow-wave leaky-wave antenna, the guiding structure that supports the leaky wave is always a periodic structure. In this type of antenna the fundamental mode is a nonradiating slow wave ($\beta > k_0$). In this

case radiation occurs from one of the space harmonics, which is a fast wave. Examples of this type of antenna include dielectric waveguide structures with metal strips or dielectric gratings (8,9).

All of the antennas just mentioned make beam forming possible only in one dimension, so that a focusing of the beam in a plane perpendicular to the waveguide axis is only possible by using an parallel array of these antennas. The leaky-wave antennas discussed here overcome this limitation.

In addition to leaky-wave antennas, a general class of antennas that is very suitable for millimeter-wave operation is the class of planar antennas. Planar antennas are easily fabricated and have the advantage of being low in profile. Furthermore, these antennas are compatible with monolithic integration with active or passive devices. Examples, include the Vivaldi antenna (10) or the linear tapered slot-line antenna (11).

In this article, a class of leaky-wave antennas known as planar dielectric leaky-wave antennas are reviewed. These antennas combine the advantages of leaky-wave antennas with the advantages of planar antennas. These leaky-wave antennas are planar in configuration, and the basic guiding structure consists of one or more dielectric layers mounted over a ground plane. Theoretical investigations by Jackson and Alexopoulos (12) showed that using two dielectric sheets (substrate and superstrate) over a ground plane can yield a high directivity pattern when using only a single radiating element, such as a dipole. The concept was then extended by Yang and Alexopoulos to include multiple dielectric sheets (13). In contrast to conventional single radiators, which have a broad beamwidth, a highly directive pattern is obtained through the excitation of leaky waves on the dielectric structure. A leaky-wave explanation for the narrow-beam effect was given by Jackson and Oliner in Ref. 14 A further analysis of these planar dielectric leaky-wave antennas was made by Ostner et al. [15], in which the role of the leaky waves, surface waves, and space waves in the determination of the radiation pattern was critically examined for both infinite- and finite-size apertures for a one-dimensional excitation problem (line-source feed). The authors also showed that these antennas have low cross-polarization (typically less than -25 dB).

In Ref. 15, a method was developed for calculating the radiation patterns from practical planar dielectric leaky-wave antennas that have a finite aperture size, either circular or rectangular in shape. In this same reference, the proposal to use these antennas in the millimeter-wave range was made for the first time, with both calculated and measured patterns presented for a leaky-wave antenna operating at 62.2 GHz, constructed from a ceramic dielectric layer.

The purpose of this article is to review the basic operating principles, design techniques, and methods of analysis for this new class of planar dielectric leaky-wave antennas. It is hoped that the present article will help stimulate the successful use of these antennas in the millimeter-wave frequency region.

Basic Properties of Planar Leaky-Wave Structures

Structure and Fundamental Properties. Planar structures consisting of dielectric layers are able to support the existence of weakly attenuated leaky waves (small attenuation constant) if they are properly dimensioned (14). The principle configuration is shown in Fig. 1 (13). The attenuation constant of the leaky waves is determined by the refractive index relationship n_2/n_1, where $n^2{}_{\mathrm{i}} = \varepsilon_{\mathrm{ri}}\,\mu_{\mathrm{ri}}$, and by the number of layers (16). A larger refractive index ratio or a larger number of layers will result in a smaller attenuation constant of the leaky waves. This, in turn, will result in a higher-gain radiation pattern (smaller beam width) from a radiating source inside the layered structure.

The structure consists of dielectric sheets arranged in pairs above a perfectly conducting metallic plate. The design process can be based on differing dielectric constants $\varepsilon_{\mathrm{ri}}$ or relative permeabilities μ_{ri}. Usually nonmagnetic (dielectric) materials will be used, because they are inexpensive and easy to work with. Therefore, the design discussion will be limited to this case.

In the alternating arrangement shown in Fig. 1, the layers alternate between lower-permittivity layers (ε_1) and high-permittivity layers (ε_2). The thickness of the first layer is twice the thickness of the other

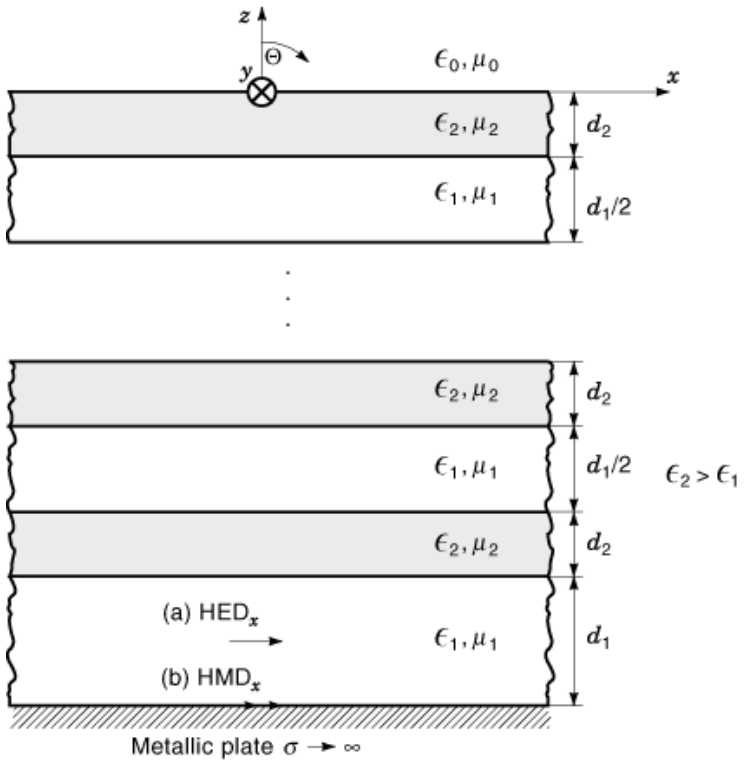

Fig. 1. Planar multilayer leaky-wave antenna configuration: (a) Excitation using a horizontal electric dipole in the x direction (HED$_x$). (b) Excitation using a horizontal magnetic dipole in the x direction (HMD$_x$).

odd-numbered layers, while all even-numbered layers have the same thickness. A high-gain antenna pattern can be produced from a source inside this structure if the following resonance conditions for the layer thicknesses d_1 and d_2 are satisfied for integers l and m (13):

$$d_1 = (2l-1)\frac{\lambda_0}{2\sqrt{n_1^2 - \sin^2\theta_p}} \tag{1a}$$

$$d_2 = (2m-1)\frac{\lambda_0}{4\sqrt{n_2^2 - \sin^2\theta_p}} \tag{1b}$$

The angle θ_p denotes the desired scan direction of the antenna beam in spherical coordinates, measured from the z axis. The structure can be designed for any scan angle, except that $\theta_p = 90^\circ$ is not possible when using an air substrate.

The excitation source inside the structure that excites the leaky waves (and hence produces the radiation pattern) can typically be modeled as an electric or magnetic line source in the two-dimensional case (17), or a horizontal electric dipole (*HED*), horizontal magnetic dipole (*HMD*), or vertical electric dipole, (*VED*) in the three-dimensional case (18) (Fig. 1 shows the *HED* and *HMD* sources). The geometry of the layer structure and, to a lesser extent, the type of source determine the shape of the radiation pattern. The radiation pattern

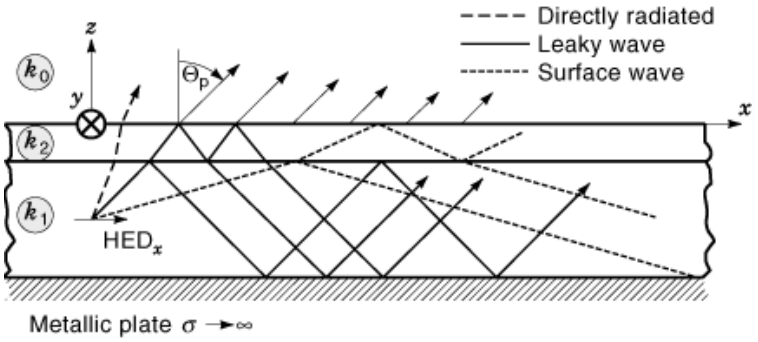

Fig. 2. Ray-optics explanation of leaky-wave propagation in a two-layer leaky-wave structure. $k_i = \omega\sqrt{\epsilon_i \mu_i}$ is the wave number for thcorresponding medium.

is a conical beam for $\theta_p > 0$, having unequal beam widths in the E and H planes. For $\theta_p = 0$, the beam is a circular pencil beam at broadside, having equal beam widths in the E and H planes (12).

The placement of the source inside the structure mainly determines the excitation amplitude of the leaky waves and hence the power density radiated at the beam peak. To radiate maximum power, an *HED* source should be positioned in the middle of the lower layer, while an *HMD* or *VED* should be positioned at the ground plane. This optimum positioning is usually desirable, since the leaky-wave (narrow-beam) pattern is then dominant over any residual direct-feed radiation, making the overall pattern more nearly that of the narrow-beam leaky-wave pattern alone.

The resonance conditions given in Eq. (1a) can be illustrated using a simple ray-optics model (in which the "rays" correspond to plane waves in the Fourier spectrum radiated by the source, propagating at different angles) (19). Figure 2 illustrates the ray-optics model for a two-layer structure. Layers 1 and 2 have low and high permittivities, respectively. If the ratio $\varepsilon_{r2}/\varepsilon_{r1}$ is chosen high enough (or if a sufficient number of layers are used in the multilayer structure of Fig. 1) a reflection coefficient $R \approx -1$ can be produced at the interface between the first and second layers (20) for a wave propagating in the first layer at an angle θ_1, where θ_1 is related to the beam angle θ_p by Snell's law. This is because the part of the layered structure that is above the first layer acts as a filter, being highly reflective to waves at angle θ_1. This reflective property is in turn due to the fact that the high-permittivity layer acts as a quarter-wave transmission line with a low characteristic impedance when Eq. (1b) is satisfied. Because of this reflective property, for waves in the first layer propagating at angle θ_1, the structure acts as an imperfect parallel-plate waveguide, effectively trapping the wave inside the first layer. Since the reflection from the interface is not perfect, there is a small leakage of power into space every time the wave reflects from the interface, with the wave partially transmitted through the upper layer and into space. Hence, the layered structure acts as a leaky parallel-plate waveguide for a wave in the first layer propagating at angle θ_1. A consequence of this is that a source inside the layered structure will excite a radial leaky mode, propagating outward from the source with a propagation constant $k_\rho = \beta - j\alpha$.

The ratio of permittivities (or number of layers) determines the amount of leakage. A structure with a higher permittivity ratio will have less leakage, meaning a smaller attenuation constant α and hence a larger effective radiating aperture. This, in turn, results in a narrower-beam radiation pattern produced by the dipole (or any other source) inside the layered structure.

The beam angle θ_p is primarily determined by the thickness of the first layer d_1. Equation (1a) specifies the required thickness in order to have a radiated beam at angle θ_p. The resonance condition in Eq. (1a) simply results in the first layer being one-half wavelength thick (using $l = 1$) with respect to the vertical wavelength λ_z at the scan angle θ_p. This is the usual resonance condition for a wave propagating in a parallel-plate

waveguide. (Any multiple of one-half wavelength will also work, but using one-half wavelength will give the thinnest possible structure.)

The determination of the electrical properties of these multilayered structures will be carried out using a full-wave analysis, described in the next section.

Full-Wave Analysis in the Spectral Domain. To calculate the electric field on the aperture ($z = 0$) the spectral-domain Green's function is used (21). The electric field at a point (x, y, z) produced by a planar source current J_s at $z = z_0$ in an infinite layered structure is given by the convolution integral

$$\boldsymbol{E}(x, y, z) = \iint [G_E(x, y, z|x', y', z_0)]\, \boldsymbol{J}_s(x', y', z_0) dx'\, dy' \quad (2)$$

in which $[G_E(x, y, z|x', y', z')]$ represents the Green's dyad for the electric field. The convolution integral can be written as a multiplication in the spectral domain, giving the relation

$$\tilde{\boldsymbol{E}}(k_x, k_y, z) = [\tilde{G}_E(k_x, k_y, z)]\tilde{\boldsymbol{J}}_s(k_x, k_y, z_0) \quad (3)$$

(The tilde denotes Fourier transform.) The electric field $E(x, y, z)$is given by the inverse Fourier transform of Eq. (3) as

$$\boldsymbol{E}(x, y, z) = \frac{1}{4\pi^2}\int_{-\infty}^{\infty}\int [\tilde{G}_E(k_x, k_y, z)]\tilde{\boldsymbol{J}}_s(k_x, k_y, z_0) e^{-j(k_x x + k_y y)} dk_x\, dk_y \quad (4)$$

The far field can be determined from the aperture fields by the stationary phase method (22), directly yielding the result

$$\boldsymbol{E}(\rho, \theta, \varphi) = \frac{jk_0}{2\pi r} e^{-jk_0 r}\{\boldsymbol{e}_\theta[\tilde{E}_x(k_x, k_y)\cos\varphi + \tilde{E}_y(k_x, k_y)\sin\varphi] + \boldsymbol{e}_\varphi \cos\theta[\tilde{E}_y(k_x, k_y)\cos\varphi - \tilde{E}_x(k_x, k_y)\sin\varphi]\} \quad (5)$$

where $\boldsymbol{e}_i$ ($i = \varphi, \theta$) denotes the unit vector and

$$\tilde{E}_x(k_x, k_y) = \tilde{G}_E^{xx}\tilde{J}_x + \tilde{G}_E^{xy}\tilde{J}_y \quad (6)$$

$$\tilde{E}_y(k_x, k_y) = \tilde{G}_E^{yx}\tilde{J}_x + \tilde{G}_E^{yy}\tilde{J}_y \quad (7)$$

$$k_x = k_0 \sin\theta\cos\varphi \quad (8a)$$

$$k_y = k_0 \sin\theta\sin\varphi \quad (8b)$$

For magnetic current sources $\boldsymbol{M}_s$, the far-field result is

$$\boldsymbol{E}(r, \theta, \varphi) = -\frac{jk_0\eta_0}{2\pi r} e^{-jk_0 r}\{\boldsymbol{e}_\theta \cos\theta\,[\tilde{H}_x(k_x, k_y)\sin\varphi - \tilde{H}_y(k_x, k_y)\cos\varphi] + \boldsymbol{e}_\varphi\,[\tilde{H}_x(k_x, k_y)\cos\varphi + \tilde{H}_y(k_x, k_y)\cos\varphi]\} \quad (9)$$

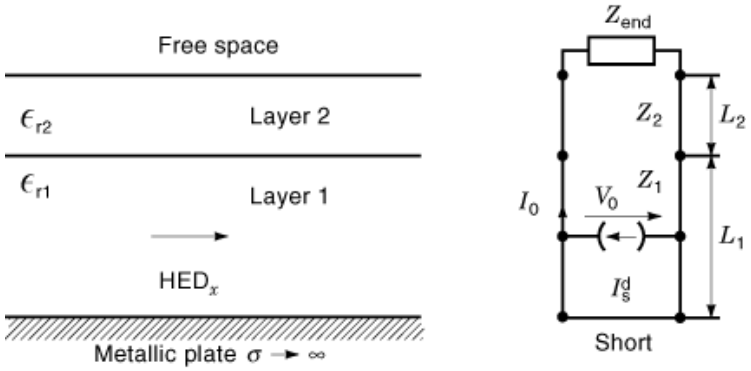

Fig. 3. Transmission-line model for a double-layered planar structure, excited using a HED_x source.

where

$$\widetilde{H}_x(k_x, k_y) = \widetilde{G}_H^{xx}\widetilde{M}_x + \widetilde{G}_H^{xy}\widetilde{M}_y \tag{10}$$

$$\widetilde{H}_y(k_x, k_y) = \widetilde{G}_H^{yx}\widetilde{M}_x + \widetilde{G}_H^{yy}\widetilde{M}_y \tag{11}$$

In these expressions a known current distribution ($\boldsymbol{J}_s$ or $\boldsymbol{M}_s$) producing the aperture fields has been assumed. This will be the case for point-dipole sources (*HED*, *HMD*, *VED*). If dipoles with finite dimensions, or other finite-size current sources are used, the current distribution will in general have to be determined using a numerical technique such as the method of moments. This will be the case, for example, if the current source is a dipole or patch of finite dimensions, or a finite-size slot in the ground plane. However, radiation patterns are, in general, not very sensitive to assumed current distributions. This property is all the more true for the present case of a source inside the leaky-wave dielectric structure, since the radiation pattern near the beam peak is almost exclusively determined by the propagation wave number of the leaky wave and not by the specific geometry of the source that is used to launch the leaky wave.

Although the calculation of the spectral-domain Green's function is well known (21), the next section presents a brief summary of the calculation procedure.

Green's Functions for Layered Media.

Network Analogy. The calculation of the fields due to sources in layered media can be done in various ways. One approach is to use various components of the Hertzian potentials (23). One disadvantage of this approach is that the coupling of the potentials at the boundaries makes the solution tedious for a structure with multiple layers (24). A simpler approach is to decompose the fields inside the structure into a continuous spectrum of TE_z and TM_z plane-wave fields (21). The two fields are coupled only at the source, with the result that each field can be modeled separately using a transmission-line model, according to the basic principles of microwave field theory (25).

In order to save space we omit the derivation and give only the results. An illustration of the transmission-line model for a two-layered structure is shown in Fig. 3. In this model the transverse components of the Fourier transform of the electric and magnetic fields are modeled as voltage and current on the transmission line. In particular, for the TM_z fields the modeling relations are

$$V^{\mathrm{TM}}(z) = \widetilde{E}_u(k_x, k_y, z) \tag{12}$$

$$I^{\mathrm{TM}}(z) = \widetilde{H}_v(k_x, k_y, z) \tag{13}$$

where the (u, v) coordinates define a rotated coordinate system in the Fourier transform (k_x, k_y) plane. In particular,

$$\boldsymbol{e}_u = \frac{\boldsymbol{e}_x k_x + \boldsymbol{e}_y k_y}{k_t}$$
$$\boldsymbol{e}_v = \boldsymbol{e}_z \times \boldsymbol{e}_u$$

where

$$k_t = \sqrt{k_x^2 + k_y^2}$$

Similarly, the TE_z modeling relations are

$$V^{TE}(z) = \tilde{E}_v(k_x, k_y, z) \tag{14}$$

$$I^{TE}(z) = -\tilde{H}_u(k_x, k_y, z) \tag{15}$$

For the TM_z case the wave impedance Z^{TM} and the phase constant β_z on a particular section of transmission line are given by

$$Z^{TM} = \frac{k_z}{\omega\epsilon} \tag{16}$$

$$\beta = k_z \tag{17}$$

The sources in the transmission-line model depend on the type of source. A horizontal current is modeled as a parallel current source, while a horizontal magnetic current or a vertical electric dipole is modeled by a series voltage source (Fig. 3 shows an *HED* source in the x direction). The general source terms for the parallel current source and the series voltage source in the TM_z model are

$$I_s^d = -\tilde{J}_u \tag{18a}$$

$$V_s^d = -\tilde{M}_v + \frac{k_t}{\omega\epsilon}\tilde{J}_z \tag{18b}$$

The corresponding relations for the TE_z case are

$$I_s^d = -\tilde{J}_v + \frac{k_t}{\omega\mu}\tilde{M}_z \tag{19a}$$

$$V_s^d = -\tilde{M}_u \tag{19b}$$

$$Z^{TE} = \frac{\omega\mu}{k_z} \tag{20}$$

$$\beta = k_z \tag{21}$$

Using the transmission-line model we can derive the transverse electric and magnetic fields at any value of z by first calculating the voltage and current in the model. This is easily done by cascading the *ABCD* matrices that relate the voltage and current at the top of a transmission-line section to the corresponding quantities at the bottom of the same section (26). In this way the voltage and current at the aperture (load Z_{end}) can be found from the voltage V_0 and the current I_0 at the source location.

In the xy plane the electric field is given as

$$\widetilde{E}_x = \widetilde{E}_u \cos\bar{\phi} - \widetilde{E}_v \sin\bar{\phi} \tag{22a}$$

$$\widetilde{E}_y = \widetilde{E}_u \sin\bar{\phi} + \widetilde{E}_v \cos\bar{\phi} \tag{22b}$$

where φ is the polar angle in the (k_x, k_y plane. Similar equations hold for the magnetic field. For a horizontal electric current source, the transmission-line voltages can be written in a convenient form as

$$V^{\text{TM}}(z) = I_{\text{s}}^{\text{dTM}} V_i^{\text{TM}}(z) \tag{23a}$$

$$V^{\text{TE}}(z) = I_{\text{s}}^{\text{dTE}} V_i^{\text{TE}}(z) \tag{23b}$$

where $V^{\text{TM}}{}_i\ (z)$ is the voltage on the TM transmission line due to a 1 A parallel current source at $z = z_0$ and similarly for $V^{\text{TE}}{}_i\ (z)$. The source terms $I^{\text{dTM,TE}}{}_{\text{s}}$ are described in Eqs. (18a) and (19a). The current on the transmission line (modeling the transverse magnetic field) can be found in a similar way.

For an *HMD* or a *VED*, the current on the transmission line due to the voltage sources $V^{\text{dTM,TE}}{}_{\text{s}}$ in Eqs. (18a) and (19a) can be represented as

$$I^{\text{TM}}(z) = V_{\text{s}}^{\text{dTM}} I_v^{\text{TM}}(z) \tag{24a}$$

$$I^{\text{TE}}(z) = V_{\text{s}}^{\text{dTE}} I_v^{\text{TE}}(z) \tag{24b}$$

where $I^{\text{TM}}{}_{\text{v}}\ (z)$ is the TM transmission line current due to a 1 V series source at $z = z_0$ and similarly for $I^{\text{TE}}{}_v$ (z).

With use of Eqs. (12) to (15), (18a), (19a), (22a), and (23a), the Fourier transform of the transverse electric fields due to a planar electric current source can be obtained as

$$\begin{bmatrix} \widetilde{E}_x \\ \widetilde{E}_y \end{bmatrix} = \begin{bmatrix} \widetilde{G}_E^{xx} & \widetilde{G}_E^{xy} \\ \widetilde{G}_E^{yx} & \widetilde{G}_E^{yy} \end{bmatrix} \begin{bmatrix} \widetilde{J}_x \\ \widetilde{J}_y \end{bmatrix} \tag{25}$$

with

$$[\,\widetilde{G}_E\,] = -\frac{1}{k_t^2} \begin{bmatrix} k_x^2 V_i^{\text{TM}} + k_y^2 V_i^{\text{TE}} & k_x k_y \left(V_i^{\text{TM}} - V_i^{\text{TE}} \right) \\ k_x k_y \left(V_i^{\text{TM}} - V_i^{\text{TE}} \right) & k_y^2 V_i^{\text{TM}} + k_x^2 V_i^{\text{TE}} \end{bmatrix} \tag{26}$$

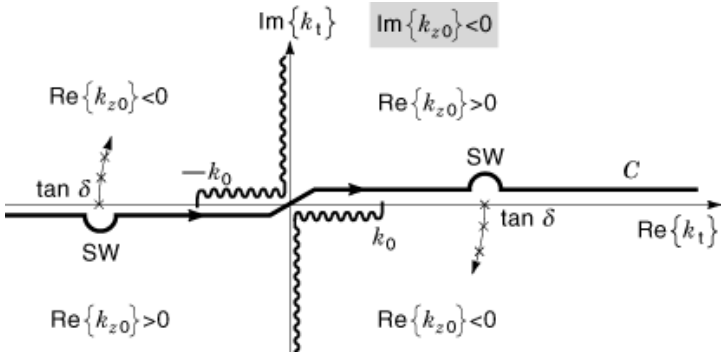

Fig. 4. Complex k_t plane, showing the integration path C in the top Riemann sheet (Im $\{k_{z0}\} < 0$). The regions Re$\{k_{z0}\} \leqslant 0$ are labeled, and the movement of the SW poles with increasing loss tangent (tan δ) is shown.

The Green's dyad G_H giving the relationship between the spectral magnetic fields $\tilde{H}_x \tilde{H}_y$ and a horizontal planar magnetic current source M_x, M_y can be written as

$$\begin{bmatrix} \tilde{H}_x \\ \tilde{H}_y \end{bmatrix} = \begin{bmatrix} \tilde{G}_H^{xx} & \tilde{G}_H^{xy} \\ \tilde{G}_H^{yx} & \tilde{G}_H^{yy} \end{bmatrix} \begin{bmatrix} \tilde{M}_x \\ \tilde{M}_y \end{bmatrix} \tag{27}$$

with

$$[\tilde{G}_H] = -\frac{1}{k_t^2} \begin{bmatrix} k_y^2 I_v^{\mathrm{TM}} + k_x^2 I_v^{\mathrm{TE}} & k_x k_y \left(I_v^{\mathrm{TE}} - I_v^{\mathrm{TM}} \right) \\ k_x k_y \left(I_v^{\mathrm{TE}} - I_v^{\mathrm{TM}} \right) & k_x^2 I_v^{\mathrm{TM}} + k_y^2 I_v^{\mathrm{TE}} \end{bmatrix} \tag{28}$$

For vertical electric dipoles the spectral magnetic field is given by

$$\begin{bmatrix} \tilde{H}_x \\ \tilde{H}_y \end{bmatrix} = \begin{bmatrix} k_y \\ -k_x \end{bmatrix} \frac{I_v^{\mathrm{TM}}}{\omega \epsilon} \tilde{J}_z \tag{29}$$

Discussion of Leaky-Wave Poles. The transmission-line terms discussed in the previous section are functions of the wave number k_t only. Hence, when performing the double integration in Eq. (4) in polar (k_t, φ) coordinates, the k_i integration will exhibit the singularities of the Green's function while the φ integration will not. In order to explore the singularities in the k_t plane, it is noted that the functional dependence of the Green's functions is related to the vertical wave number $k_{zi} = \sqrt{k_i^2 - k_t^2}$. The Green's function is an even function of k_{zi} for all regions except the top air region ($k_i = k_0$) (27). The Green's function is therefore analytic at $k_t = k_i$ for all k_i corresponding to the dielectric layers. The Green's function is not an even function of the wave number k_{z0}, and hence a square-root type of branch point appears at $k_t = \pm k_0$ in the k_t plane due to the double-valued nature of the square root in the calculation of k_{z0}. The introduction of branch cuts (wavy lines in Fig. 4) yields well-defined Riemann sheets. If the branch cuts are chosen along the contour described by Im $\{k_{z0}\} = 0$ (the "Sommerfeld" choice of branch cuts), then one Riemann sheet (denoted as the "top" sheet) describes Im $\{k_{z0}\} < 0$ and the other sheet (the "lower" sheet) describes Im $\{k_{z0}\} > 0$. The top sheet is also denoted as the "proper" sheet, since the waves decay at $z = \infty$, that is they are "proper," whereas the bottom sheet is termed the "improper" sheet due to the "improper" (exponentially growing) behavior at $z = \infty$. The Sommerfeld radiation

condition will be satisfied if the path of integration in the k_t plane stays on the top Riemann sheet. The path of integration shown in Fig. 4, which does not cross the branch cuts, is one such path.

Another consideration is what parts of the complex k_t plane correspond to outward-propagating waves ($\mathrm{Re}\{k_{z0}\} > 0$) and what parts correspond to inward-propagating waves ($\mathrm{Re}\{k_{z0}\} < 0$). For the top (proper) Riemann sheet, the regions are indicated in Fig. 4. As seen, the first and third quadrants are the outward regions. The path shown in Fig. 4 remains in the outward region of the k_t plane, so that the solution consists of physical outward-going waves, as expected.

Next, the pole singularities of the Green's function are considered. Three types of poles occur, corresponding to surface waves (SWs), improper surfaces waves (ISWs), or leaky waves (LWs), depending on their location in the two-sheeted complex k_t plane. The pole singularities correspond to guided modes that can propagate on the layered structure. The surface-wave (SW) modes always correspond to physical modes that are launched by the source, while the improper surface-wave (ISW) modes do not correspond to physical modes. The leaky-wave (LW) modes may correspond to physical modes (as will always be the case for a properly designed leaky-wave antenna structure). This point will be discussed in more detail later.

For a lossless structure, the SW poles at $k_t = k_{tp}$ are situated on the real axis in the regions $k_0 < k_{tp} < \max k_i$ and $-\max k_i < k_{tp} < -k_0$. Introducing losses, the SW poles move into the fourth and second quadrants, respectively. This defines the way the path is deformed around the SW poles for the lossless case, as shown in Fig. 4. By closing the contour in the lower half plane, the integration along the path C in Fig. 4 is seen to be equivalent to an integration around the branch cut in the fourth quadrant plus a residue contribution from an integration around the SW pole singularities on the top sheet in the fourth quadrant. If the integration is used to calculate the fields on the aperture (a convenient Huygen surface for determining the far-field pattern), the aperture field is then represented in terms of a surface-wave field (from the pole residues) plus a "continuous spectrum" field (from the branch-cut integration).

In contrast to the SW poles, the ISW and LW poles are located on the bottom (improper) Riemann sheet, and hence the corresponding guided modes are improper, that is, the fields increase exponentially in the z direction. The ISW poles are located on the real axis in the region $k_{tp} > k_0$ (with symmetrically located poles in the region $k_{tp} < -k_0$). These solutions correspond to waves that are slow with respect to the free-space wave number but increase transversely. These solutions are generay regarded as having no physical significance. Although an ISW solution is not physically significant, it mathematically represents the continuation of a proper SW mode below the cutoff frequency of the surface wave. All of the SW modes of a layered structure above a ground plane have a cutoff frequency except for the dominant TM_0 mode, which remains a proper SW mode down to zero frequency (28). Hence, all SW modes except for the TM_0 mode will eventually become ISW modes as the frequency is lowered.

The LW poles are also located on the improper sheet of the k_t plane, but the wavenumber (pole location) is complex due to radiation loss. The LW poles that are responsible for the radiation pattern of the dielectric leaky-wave antenna are located in the fourth quadrant of the bottom Riemann sheet. If a LW pole is located in the fast-wave region, $\beta = \mathrm{Re}\{k_{tp}\} < k_0$, the pole is "close" to the path of integration on the Riemann surface. In this case the pole can have a significant influence on the integration if the pole is sufficiently close to the real axis (small attenuation constant) and the residue is sufficiently large (the mode is excited sufficiently by the source). In this case the continuous-spectrum aperture field (given by the path integral around the branch cut) will resemble the field of the leaky mode alone (given by the residue contribution of the LW pole). On the other hand, if the pole is located in the slow-wave region, $\beta = \mathrm{Re}\{k_t\} > k_0$, the pole will never be close to the integration path on the Riemann surface and therefore will never have a very significant influence on the path integration, regardless of how small the attenuation constant is. A LW pole in the fast-wave region is therefore said to be in the "physical" region, whereas a LW pole in the slow-wave region is said to be in the nonphysical or "spectral-gap" region (29). Near the spectral-gap boundary, where $\beta \approx k_0$, the distinction between a physical and a nonphysical LW mode becomes rather blurred (this corresponds to a leaky-wave antenna radiating near end fire).

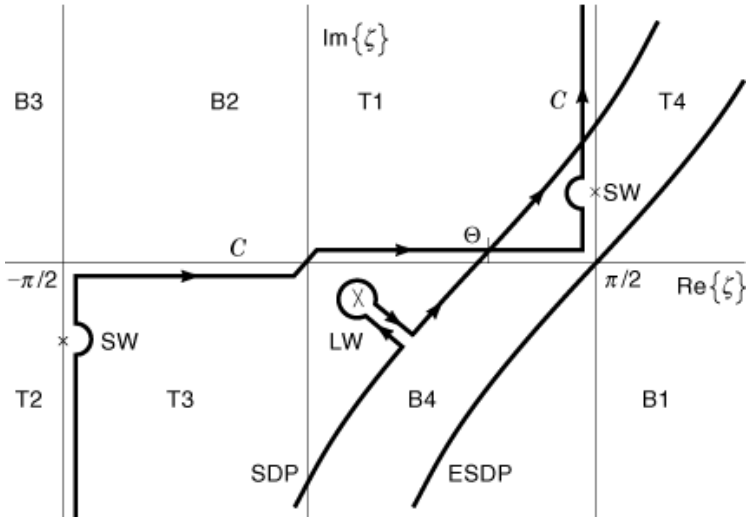

Fig. 5. Steepest-descent ζ plane, showing the original path C, the steepest-descent path for an arbitrary angle θ, and the extreme steepest-descent path ESDP. The regions are labeled to indicate the corresponding quadrants of the k_t plane in the mapping. The SW poles and the location of a typical LW pole are also shown.

A LW mode represents the continuation of an ISW mode at lower frequencies. Typically, a proper SW mode becomes an ISW mode for a finite frequency span below the cutoff frequency. For still lower frequencies, the ISW mode becomes a LW mode with a complex propagation constant. This transition will occur for most of the modes on a grounded layered dielectric structure. However, the TE_1 mode (the lowest-order TE mode) is a notable exception. This mode remains an ISW mode for all frequencies below the cutoff frequency.

At the onset of leakage (where the mode first becomes complex), the LW mode is always a slow wave, and is thus nonphysical. However, as the frequency is lowered, the phase constant of the LW mode begins to decrease. If the wave becomes a fast wave at a sufficiently low frequency, the LW mode will be a physical radiating mode.

Representation in the Steepest-Descent Plane. Using the transformation

$$k_t = k_0 \sin\zeta \tag{30a}$$

$$k_z = k_0 \cos\zeta \tag{30b}$$

the branch point at $k_i = k_0$ (mapped to the point $\zeta = \pi/2$) will be eliminated, and the Green's function in the ζ plane becomes analytic except for pole singularities. The various quadrants of the two Riemann sheets in the k_t plane are mapped onto semi-infinite strips of width $\pi/2$, as illustrated in Fig. 5. The notation T_i denotes the region mapped from the ith quadrant of the top sheet, and B_i similarly denotes a mapping from one of the quadrants in the bottom sheet.

The real-axis path of integration C in Fig. 4 is mapped onto the corresponding path labeled C in Fig. 5. When using the method of steepest descents to evaluate the far-field pattern, the path in the steepest-descent plane is deformed into the steepest-descent path (SDP), shown in Fig. 5 (27). A saddle point occurs at $\zeta = \theta$, where θ is the observation angle measured from the z axis in spherical coordinates. When evaluating the aperture field at $\theta = \pi/2$, the SDP passes through the point $\zeta = \pi/2$. This particular path is referred to as the

extreme steepest-descent path (*ESDP*). The *ESDP* path separates the strip B4 into a fast-wave region (to the left of the path) and a slow-wave region (to the right of the path). Any LW poles in the fast-wave region are captured by the deformation to the ESDP, while poles in the slow-wave region are not captured. All SW poles on the line $\zeta_r = \pi/2$ are also captured by the path deformation. The aperture field can therefore be represented as the sum of a surface-wave field and a continuous-spectrum field, with the continuous-spectrum field further represented as the sum of a leaky-wave field (due to the captured LW poles) plus a "space-wave" field, defined as the contribution coming from the *ESDP* integration. An asymptotic analysis reveals that the space-wave field on the aperture from a dipole excitation decays with radial distance ρ as ρ^{-2}. The LW field, on the other hand, decays with radial distance ρ as $\rho^{-1/2}\, e^{-\alpha\rho}$. If the attenuation constant α is small, the LW field may dominate the space-wave field for considerable distances from the source, and form the major portion of the continuous-spectrum aperture field. In this case the radiation pattern of the antenna will be due essentially to the leaky wave.

Frequency Behavior of the Leaky-Wave Structure. In this section the migration of the leaky-wave poles in the steepest-descent plane as frequency changes will be considered. The determination of the pole location is done using the transverse-resonance method (30), in which the equation

$$Z_{\mathrm{b}}\left(k_{\mathrm{t}}\right) + Z_{\mathrm{a}}\left(k_{\mathrm{t}}\right) = 0 \qquad (31)$$

is solved numerically for k_{t}. In this equation Z_{b} is the impedance looking below into the dielectric layers at the air–dielectric boundary on the transmission-line model, and Z_{a} is the impedance looking above, that is, the characteristic wave impedance of free space for a given wavenumber k_{t}. These impedances have been presented earlier for both TE and TM modes. A real (and proper) solution of Eq. (31) describes a SW pole, whereas a complex solution describes a LW pole.

To designate the LW poles, the same mode numbers that describe the corresponding surface waves (above the cutoff frequency) will be used. For example, the TE_2 leaky-wave mode is the continuation of the TE_2 surface-wave mode as the frequency is lowered sufficiently below the cutoff frequency of this mode. In general, the mode designation is TM_n, $n = 0,1,2, \ldots$ and TE_n, $n = 1,2,3, \ldots$. Since the TM_0 surface-wave mode has a zero cutoff frequency and the TE_1 pole is always an ISW mode moving on the $\mathrm{Re}\{\zeta\} = \pi/2$ axis, the TM_1 and TE_2 modes are the lowest possible LW modes for the layered dielectric structure.

For the dielectric layer leaky-wave antenna, there is always a pair of leaky-wave modes that are responsible for the narrow-beam pattern, a TE mode and a TM mode (14). These two leaky-wave modes are referred to as the *dominant* leaky modes, since they typically have an attenuation constant that is considerably less than that of the other leaky modes [assuming that Eqs. (1a) are satisfied, so that the structure acts as a narrow-beam leaky-wave antenna]. The TM leaky-wave mode is responsible for the narrow-beam radiation in the *E*-plane, while the TE mode is responsible for the *H*-plane beam. When Eqs. (1a) are satisfied for a scanned beam ($\theta_{\mathrm{p}} > 0$), the two leaky-wave modes have approximately the same phase constant β, given approximately by $\beta \approx k_0 \sin\theta_{\mathrm{p}}$, but may have somewhat different attenuation constants α. This results in a different beamwidth in the two principal planes. For a broadside beam ($\theta_{\mathrm{p}} = 0$) both LW modes have approximately the same β and α, and furthermore, $\beta \approx \alpha$ (14).

It is interesting to note that both a TE and a TM leaky-wave mode are simultaneously required in order to produce a narrow beam at broadside (18). A pair of modes with equal amplitudes is automatically excited when Eqs. (1a) are satisfied with $\theta_p = 0$, producing a narrow beam at broadside. For a scanned beam [$\theta_{\mathrm{p}} > 0$ in Eqs. (1a)], a single TM leaky-wave mode will produce a narrow-beam pattern in the *E* plane, while a single TE leaky-wave mode will produce a narrow-beam pattern in the *H* plane. Both modes are excited when Eqs. (1a) are satisfied with $\theta_{\mathrm{p}} > 0$, although with unequal amplitudes.

The specific modes that are dominant in determining the pattern near θ_{p} depend on the number of layers in the structure. For the two-layer structure shown in Fig. 3, the dominant LW modes are the TM_2 and TE_2

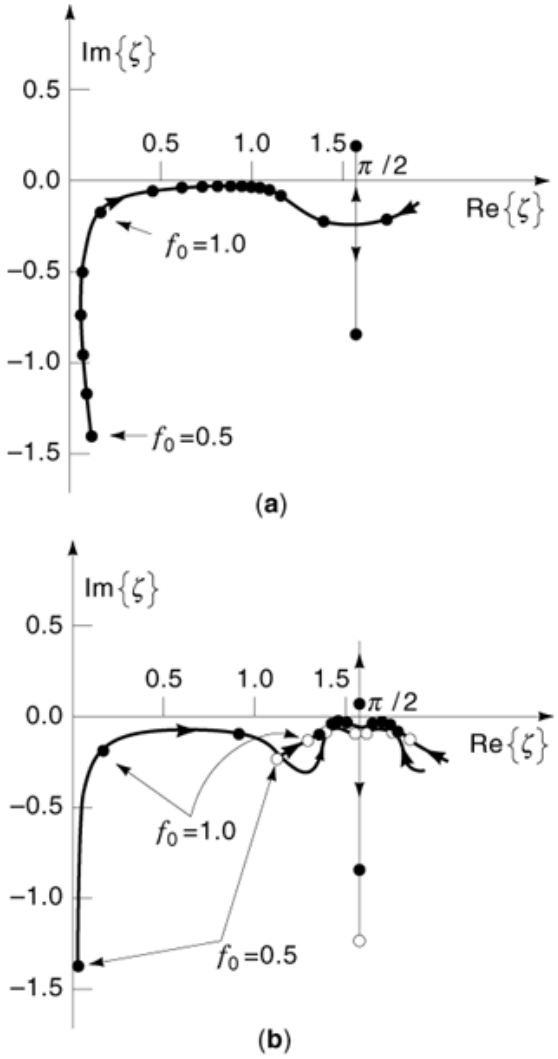

Fig. 6. Migration of the dominant (a) TE leaky-wave mode (TE_2) versus normalized frequency $f_0 = f/f_b$ and (b) TM leaky-wave mode (TM_2,$), and the TM_1 (○) leaky-wave mode versus normalized frequency for a two-layered structure. $\varepsilon_{r1} = 1.0$ and $\varepsilon_{r2} = 10.8$.

modes. More details concerning the nature of the LW modes and their relation to the radiation pattern may be found in Refs. 14 and 18.

In Fig. 6 the location of the dominant LW poles are shown for the two-layer structure in Fig. 3. The lower layer is air, while the upper layer has a relative permittivity of 10.8. The pole location is plotted as a function of normalized frequency f_0, which is defined to be the operating frequency f vided by the frequency f_b at which Eqs. (1a) are satisfied, assuming that the structure has been designed so that these equations are both satisfied for $\theta_p = 0$ (broadside) at some frequency f_b. In Fig. 6(b) the location of the TM_1 mode is also shown, in addition to the TM_2 mode.

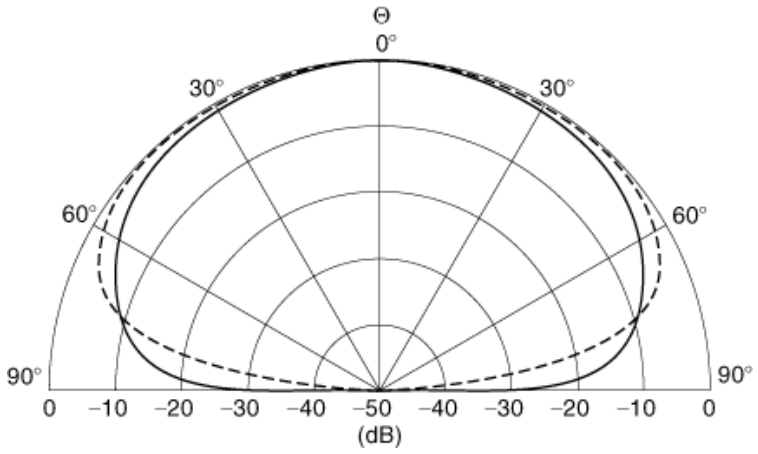

Fig. 7. Far-field pattern for the two-layered structure with $\varepsilon_{r1} = 1.0$, $\varepsilon_{r2} = 10.8$, and $\theta_p = 0$, excited from an HED_z dipole at $z_0 = -(d_2 + d_1/2)$ at a normalized frequency of $f_0 = f/f_b = 0.5$. (—E plane;—, H plane).

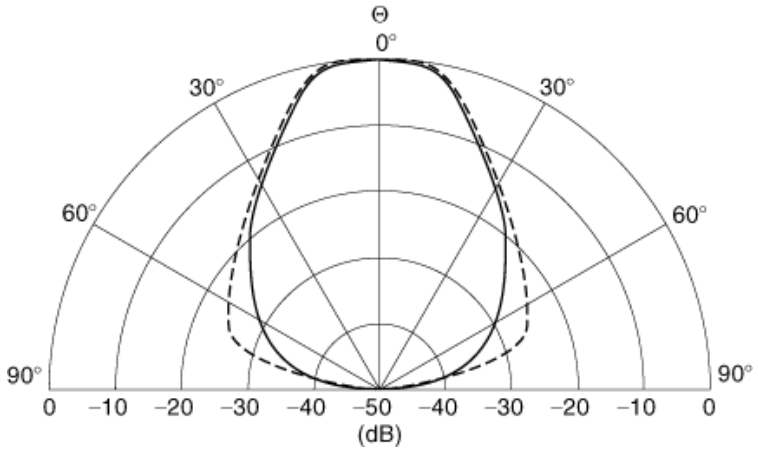

Fig. 8. Far-field pattern for the two-layered structure with $\varepsilon_{r1} = 1.0$, $\varepsilon_{r2} = 10.8$, and $\theta_p = 0$, excited from an HED_z dipole at $z_0 = -(d_2 + d_1/2)$ at a normalized frequency of $f = f/f_b = 1.0$. (—E plane;—, H plane).

For frequencies $f \ll f_b$ the LW poles TE_2 and TM_2 are far away from the real axis, and the excited leaky waves are therefore strongly attenuated. Their contribution to the radiation pattern can therefore be neglected, and the radiation characteristics are not too different from a simple dipole in free space above a ground plane. This is seen in Fig. 7, which shows the E- and H-plane patterns for the case $f_0 = f/f_b = 0.5$ for a HED_x source in the middle of the lower layer. This type of pattern behavior is also typical for the usual case of single-layer microstrip antennas, when the substrate thickness is small compared to a wavelength.

In the range $f \approx f_b$, the dominant LW poles are close to the origin of the ζ plane at an angle of approximately -45°, corresponding to $\beta \approx \alpha$. A narrow-beam broadside pattern results, as shown in Fig. 8. Because the lower layer is air, the TM_1 mode contributes to the radiation pattern in the region $\theta \approx 90^\circ$. For a higher-permittivity bottom layer, the TM_1 mode would be above cutoff (a surface-wave mode) and would not contribute to the radiation pattern.

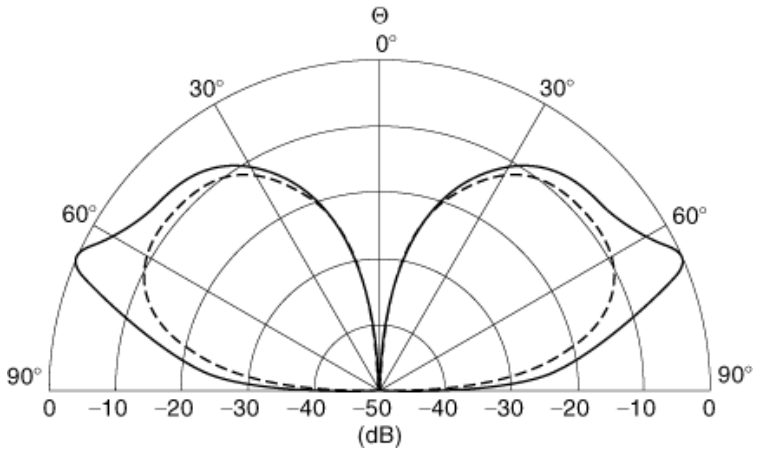

Fig. 9. Far-field pattern for the two-layer structure with $\varepsilon_{r1} = 1.0$, $\varepsilon_{r2} = 10.8$, and $\theta_p = 0$, excited from an HED_z dipole at $z_0 = -(d_2 + d_1/2)$, at a normalized frequency of $f_0 = f/f_b = 2.0$. (—E plane;—, H plane).

As the frequency increases beyond $f = f_b$, the beam scans as shown in Fig. 9. The radiation pattern is now a conical beam at a scan angle θ_p . As the beam begins to scan, the dominant LW poles migrate closer to the real ζ axis. The main beam angle is then accurately predicted by $\theta_p \approx \mathrm{Re}\{\zeta_p\}$. As Fig. 6 shows, the dominant TE LW pole is closer to the real axis than the TM pole is (at least for scan angles that are not too close to endfire). This implies less attenuation of the TE leaky-wave pole, which results in a narrower beam in the H plane (see Fig. 9). In addition, the TM poles migrate considerably more slowly to the $\mathrm{Re}\{\zeta\} = \pi/2$ axis than the dominant TE mode does as frequency increases. This means that the main beam directions in the E and H planes will change somewhat for larger frequencies. This effect is noticed in Fig. 9. [At a given frequency, however, the main beam directions will be the same, provided the structure is designed according to Eqs. (1a)]

As the frequency continues to increase, each LW pole merges at $\mathrm{Re}\{\zeta\} = \pi/2$ with its conjugate image to become a pair of ISW mode poles. One of these poles moves up along the $\mathrm{Re}\{\zeta\} = \pi/2$ axis and crosses the real ζ axis to become a proper SW solution. The other pole moves continuously downward, remaining a nonphysical ISW solution.

To conclude, for $f \leq f_b$ an approximately circularly symmetric pattern will be generated, which radiates in the broadside ($\theta = 0^\circ$) direction when the structure has been designed for a scan angle of $\theta_p = 0^\circ$ at the operating frequency. With increasing frequency the pattern starts to scan, and a scanned conical beam is produced that radiates in the direction $\theta \approx \mathrm{Re}\{\zeta\}$. Although a scanned beam can be produced in this manner by simply changing frequency, the narrowest scanned beam will be obtained at a given operating frequency by designing the structure using Eq. (1a) with the desired scan angle θ_p.

If the dielectric constant of the upper layer in the two-layer structure is increased, the pole migration shows similar behavior, except that the poles are closer to the real axis. This means that the pattern has a smaller beamwidth, and therefore a higher directivity is realized. If the dielectric constant of the lower layer is increased, the opposite occurs, due to the reduction of the refractive-index ratio. If the dielectric constant of the lower layer is higher than 2.0, the TM_1 mode becomes a SW mode and no longer disturbs the pattern for larger angles θ, as it does for the case of an air substrate. In this case only the TE_2 and TM_2 poles determine the radiation pattern. For this case the pole migration is also smoother near end fire, lacking the "bump" near the $\mathrm{Re}\{\zeta\} = \pi/2$ line seen in Fig. 6, which is characteristic of the air–substrate case. This in turn results in main lobes in the E plane and H plane that behave similar up to large scan angles. However, one disadvantage

of using higher-permittivity substrates is that the existence of the TM_1 surface wave will result in increased losses if it is excited.

For most applications a scan angle up to 45° is sufficient, so that the lower layer can be chosen to be air. This structure has the least dielectric losses and SW losses (only the dominant TM_0 mode is a SW, for $\theta_p = 0°$ and $f = f_b$) and is the easiest and least expensive structure to build.

Increasing the number of layers according to Fig. 1 yields a structure with less attenuation for the dominant leaky waves (16) and therefore a higher directivity. But fabrication tolerances and expense may limit the use of such structures.

Analysis of One-Dimensional Dielectric Leaky-Wave Antennas

Aperture Field. The aperture field at the top interface of the dielectric leaky-wave antenna is very important, since this field can be used to directly calculate the far-field radiation pattern of the antenna. This includes calculating the pattern for a practical antenna with a truncated substrate, providing an ideal absorber termination is assumed (31). A study of the aperture field also reveals many interesting features about the nature of the leaky-wave antenna. In order to keep the discussion as simple as possible, the aperture field will be calculated and discussed for a one-dimensional leaky-wave antenna in this chapter. The antenna structure is that shown in Fig. 2, except that the *HED* dipole source is replaced by an infinite electric line source parallel to the y axis. In this case the aperture field is only a function of x. Although this assumption may seem like a restrictive idealization, a very practical type of one-dimensional leaky-wave antenna can be realized in practice, based on the line-source excitation. This will be discussed later.

The electric field on the aperture excited by the line source is polarized in the y direction (a TE_z field), and consists of a superposition of a radiation (continuous-spectrum) field $E^{\text{rad}}{}_y$ and a surface-wave field $E^{\text{SW}}{}_y$. The radiation field can be further decomposed into a space-wave field $E^{\text{SP}}{}_y$ and a leaky-wave field $E^{\text{LW}}{}_y$, as discussed in the previous section and explained in Ref. 17 In contrast to the space-wave field, which involves an integration over wavenumbers (an integration along the *ESDP* path in Fig. 5), the surface- and leaky-wave aperture fields have a discrete spectrum. Although an infinite number of leaky-wave modes exists (since there are always an infinite number of surface waves below cutoff at any given frequency), the analysis can be limited to a consideration of only the dominant leaky waves, because most of the other leaky waves have a high attenuation constant; these highly attenuated waves have little effect on the aperture field and therefore have negligible influence on the radiation pattern. The number of surface waves is limited as well to a consideration of only the TE_1 surface wave, since this is the only TE surface wave that exists on the two-layer structure for the frequencies of interest.

The tangential electric field due to a general source can be written as

$$\boldsymbol{E}(x, y, z) = \frac{1}{4\pi^2}\iint_{-\infty}^{\infty}\left[\widetilde{G}_E(k_x, k_y, z)\right]\widetilde{\boldsymbol{J}}_s(k_x, k_y, z_0)e^{-j(k_x x + k_y y)}\,dk_x\,dk_y \tag{32}$$

as discussed earlier. This equation can be simplified for the case of a line-source excitation by using the spatial-domain ⟷ Fourier transform identity

$$\boldsymbol{J}_s(x, y) = \boldsymbol{e}_y\delta(x)e^{-jk_{y0}y} \longleftrightarrow \widetilde{\boldsymbol{J}}(k_x, k_y) = \boldsymbol{e}_y 2\pi\delta(k_y - k_{y_0}) \tag{33}$$

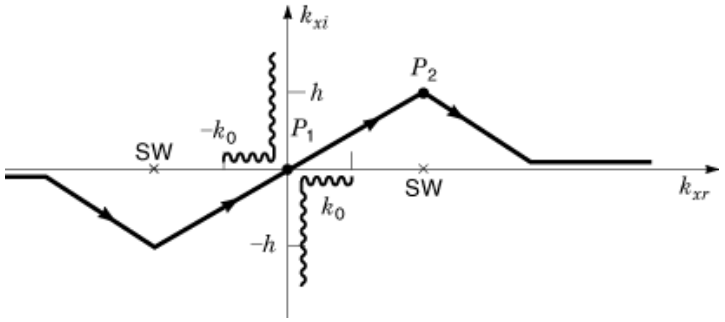

Fig. 10. Path of integration in the complex k_z plane that is used to calculate the total field on the aperture with the chirp-z transform.

The current $\boldsymbol{J}_s\ (x, y)$ describes a unit-amplitude infinite electric line source having a uniform progressive phase shift in the y direction, described by the phase constant k_{y0}. For an electric line source with a constant phase, $k\mathrm{y}_0 = 0$. In this case the electric field has only a $\boldsymbol{e}_y$ component (and hence is TE_z. The resulting expression for the aperture field ($z = 0$) is then

$$E_y(x, y, 0) = \frac{1}{2\pi} \int_{-\infty}^{\infty} \tilde{G}_E^{yy}(k_x, 0, 0) e^{-jk_x x}\, dk_x \qquad (34)$$

The spectral-domain Green's function component $\tilde{G}_{yy}^{\tilde{J}E}$ can be found analytically using the network model described earlier.

An analytical evaluation of the integral in Eq. (34) is in general not possible. However, as described in Ref. 17, the chirp- z transform (CZT) can be used to evaluate the integral efficiently, and hence compute the aperture field, for a large number of aperture points simultaneously (32, 33). A description will be given next for this method.

The integration is taken along a piecewise-linear path in the complex k_x plane, shown in Fig. 10. This path, which is equivalent to that shown in Fig. 4, consists of three different linear segments in both the first and third quadrants. The piecewise-linear path allows for a convenient application of the CZT technique. To illustrate the CZT technique, the integration along one part of the path, from P_1 to P_2, is considered. The integration then involves the following type of integral,

$$I = \int_{P_1}^{P_2} f(k_x) e^{-jk_x x}\, dk_x \qquad (35)$$

Using the substitution $k_x = P_1 + cs$, with c a complex and s a purely real number, we obtain

$$I = c e^{-jP_1 x} \underbrace{\int_0^{s_0} f(s) e^{-jcsx}\, ds}_{S} \qquad (36)$$

Using discrete sample points $s = n\ \Delta\ s$ to numerically evaluate the integral, and also defining discrete aperture calculation points $x = x_0 + k$ Delta; x, the integral S appearing in the above expression can be

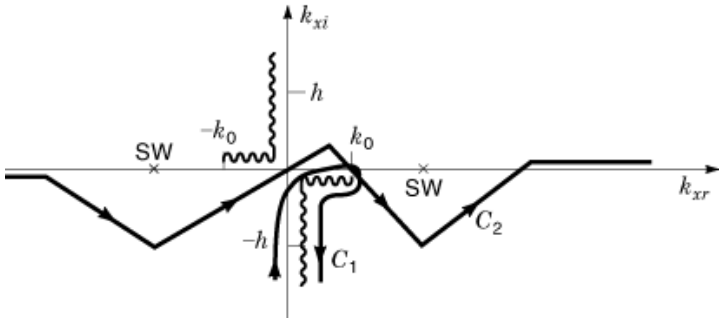

Fig. 11. Paths of integration in the complex k_z plane for calculating the radiation (continuous-spectrum) field on the aperture. The chirp-z transform is performed along the integration path C_2.

written as

$$S(k) = \sum_{n=0}^{N-1} f(n) \underbrace{e^{-jcx_0\Delta sn}}_{A^n} \underbrace{e^{-jc\Delta sn\Delta xk}}_{W^{nk}} \tag{37}$$

Using the substitution of Bluestein (34)

$$nk = \tfrac{1}{2}\left[n^2 + k^2 - (n-k)^2\right] \tag{38}$$

we have

$$S = W^{k^2/2} \sum_{n=0}^{N-1} \underbrace{f(n)A^n W^{n^2/2}}_{g(n)} W^{-(k-n)^2/2} \tag{39}$$

This equation represents a linear convolution of the form (35)

$$S = W^{k^2/2} g(n) * W^{-n^2/2}$$

which can be efficiently calculated using two direct and one inverse fast fourier transforms (*FFT*s). A much more complete description of this method can be found in Refs. 32 and 36.

Using this method, the discretization is not restricted to the special case

$$\Delta k_x \Delta x = 2\pi/N \tag{40}$$

as it would be when using a conventional *FFT*, but can chosen to be arbitrary, as long as the sampling condition

$$\mathrm{Re}\{\Delta k_x\} < \pi/a \tag{41}$$

is fulfilled, where $2a$ is the aperture size over which the field is to be calculated. This condition avoids aliasing in the field calculation.

A further decomposition of the total field into the component wave types make possible an investigation of the influence of the different components on the total aperture field and the radiation pattern. The total field is first decomposed into the radiation (continuous-spectrum) field and the surface-wave field. The radiation field is given as the integration along the branch cut (37), shown by the integration path C_1 in Fig. 11. This integration path is equivalent to the piecewise linear path C_2, which is convenient for application of the CZT.

The subtraction of the radiation aperture field from the total aperture field gives the surface-wave field on the aperture. Alternatively, the surface-wave field can be calculated using the residue at the pole location on the positive real axis.

The decomposition of the aperture radiation field into a space-wave field and a leaky-wave field is also very convenient for the physical interpretation of the aperture field. As discussed earlier, the most direct definition of the leaky-wave aperture field is the field arising from the residue contribution of the leaky-wave poles captured during the path deformation to the extreme steepest-descent path (*ESDP*) in the steepest-descent plane (see Fig. 5). The space-wave field is then given by the integration along the *ESDP* path. Although this definition of leaky-wave and space-wave aperture field is usually satisfactory, it suffers from the disadvantage that the leaky-wave field is discontinuous as the leaky-wave pole crosses the ESDP. Of course, the space-wave field is also discontinuous by the same amount, so that the radiation field is continuous as the pole crosses the ESDP. Nevertheless, it is possible to introduce a *transition function* into the definition of the leaky-wave and space-wave fields so that these fields change smoothly as the pole crosses the ESDP. The definition of the transition function is somewhat arbitrary; one physical-based requirement is that the transition function should be essentially unity when the leaky-wave pole is far to the left of the *ESDP* in strip B4 (see Fig. 5), and essentially zero when the pole is far to the right of the *ESDP* in strip B4. The definition proposed in Ref. 17 is based on outward power flow from the aperture for the leaky wave. The transition function is defined to be the ratio of the real power per unit area flowing outward from the aperture to the magnitude of the total complex power flowing outward per unit area from the aperture. A simple calculation gives the transition function $T(\zeta_p)$ as

$$T(\zeta_p) = \frac{1}{\sqrt{1 + \tan^2 \mathrm{Re}\{\zeta_p\} \tanh^2 \mathrm{Im}\{\zeta_p\}}} \tag{42}$$

where ζ_p is the pole location in the steepest-descent plane. The transition function is used as a multiplicative factor to modify the definition of the leaky-wave aperture field, which then also affects the calculation of the space-wave aperture field. The aperture fields, accounting for the transition function, are defined as

$$E_y^{\mathrm{LW}} = -jT(\zeta_p)\,\mathrm{Res}\{\widetilde{G}_E^{yy}(k_{xp})\}e^{-jk_0|x|\sin\zeta_p} \tag{43}$$

$$E_y^{\mathrm{SP}} = E_y^{\mathrm{CS}} - E_y^{\mathrm{LW}} \tag{44}$$

where ζ_p is the pole location in the steepest-descent plane and $E^{\mathrm{CS}}{}_y$ is the continuous-spectrum (radiation) aperture field, obtained from an integration along the path C_2 in Fig. 11. These definitions reduce to the customary ones if $T(\zeta_p)$ is taken as unity for a leaky wave in the fast-wave region ($\beta < k_0$) and zero for a leaky wave in the slow-wave region ($\beta > k_0$). In this case the leaky-wave field exists only when the leaky-wave pole is captured by the steepest-descent path (see Fig. 5) and is then defined to be the residue contribution of the leaky-wave pole to the integral in Eq. (34). With the inclusion of the transition function in the definitions just given, the leaky-wave field exists for any complex leaky-wave pole location. However, the amplitude of the leaky-wave field decreases as the leaky-wave pole enters the slow-wave region, with the effects of the pole on the path of integration being shifted to the space-wave aperture field rather than the leaky-wave aperture field.

These definitions of leaky-wave and space-wave aperture fields are used to calculate the different field components of the one-dimensional leaky-wave antenna shown in Fig. 12. This antenna consists of two dielectric layers above a ground plane with an infinite electric line source inside the lower (substrate) layer. The layer thicknesses are dimensioned according to the resonance condition given in Eq. (1a). This antenna produces a

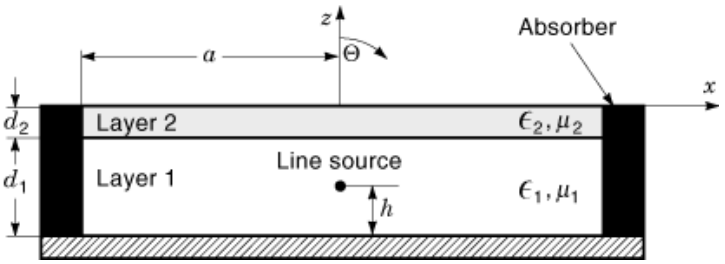

Fig. 12. Geometry of the one-dimensional leaky-wave antenna, consisting of two dielectric layers above a ground plane. The relative dielectric constants are $\varepsilon_{r\ 1} = 2.1$ and $\varepsilon_{rz} = 10.8$. The line source is located in the middle of the substrate at $h = d_1/2$.

bidirectional pattern at angles $\theta = \pm\,\theta_p$ when $\theta_p > 0^\circ$. The substrate (lower layer) is Teflon with $\varepsilon_{r1} = 2.1$, and the superstrate (upper layer) has a relative permittivity of $\varepsilon_{r2} = 10.8$. The line source is placed in the middle of the substrate to achieve maximum excitation of the dominant TE_2 leaky wave, as discussed previously.

Figure 13(a) shows the total field, the radiation (continuous-spectrum) field, and the surface-wave field on the aperture for a scan angle of $\theta_p = 45^\circ$. Because lossless dielectric layers are assumed, the magnitude of the surface-wave field is a constant. The oscillation of the total field is caused by interference between the radiation and surface-wave fields.

Figure 13(b) shows the radiation aperture field further decomposed into the leaky-wave field and the space-wave field. The radiation field is seen to be well approximated by the leaky-wave field out to very large distances with a very small space-wave field. Hence, over the plotting range shown, the radiation field is exponentially decaying due to the attenuation of the dominant TE_2 leaky wave, which has a propagation wavenumber $k_{xp} = \beta - j\alpha = (0.717 - j\,0.059)k_0$. The dominant nature of the leaky-wave field is characteristic of a well-designed leaky-wave antenna, where the radiation pattern is essentially determined by the leaky-wave aperture field alone.

If the scan angle is increased to larger angles the space wave becomes stronger relative to the leaky wave (17). In fact, for $\theta_p = 90^\circ$ the leaky-wave field is zero because the TE_2 mode is then at cutoff, corresponding to $\zeta_p = \pi/2$. At this point the residue of the pole is zero. (Furthermore, the transition function is zero whenever the pole is an improper surface-wave solution, on the $\mathrm{Re}\{\zeta\} = \pi/2$ line.) A narrow-beam pattern can still be produced for large scan angles, in fact even for $\theta_p = 90^\circ$ (12). However, for these scan angles the narrow-beam pattern is due to the space-wave aperture field rather than the leaky-wave aperture field (17). Practical use of these antennas for large scan angles is difficult, however, because a very large aperture size is necessary to attenuate the space-wave field fully (which does not decay exponentially as the leaky-wave field does).

Far-Field Analysis. To calculate the far-field radiation pattern of the one-dimensional leaky-wave antenna, the Fourier transform of the aperture field is calculated (22). To simulate the case of a finite aperture, extending from $x = -a$ to $x = a$, ideal absorbers at the boundaries are assumed. By definition, these ideal absorbers null the tangential electric field on the $z = 0$ aperture plane outside of the physical aperture, without disturbing the field inside the physical aperture, which is calculated assuming an infinite aperture. That is, the ideal absorbers perfectly absorb the aperture field incident from the line source without producing any reflections. The normalized radiation pattern of the finite-aperture antenna, $E^{\mathrm{fin}}{}_y(\theta)$, is therefore calculated from the Fourier transform of the aperture field $E^{\mathrm{fin}}{}_y(x)$, which is the aperture field of the infinite structure multiplied by a window function to null the field in the region $|x| > a$. The far-field radiation pattern is then given as

$$E_y^{\mathrm{fin}}(\theta) = \cos\theta \int_{-\infty}^{\infty} E_y^{\mathrm{fin}}(x, 0) e^{jk_{x0}^x}\, dx \qquad (45)$$

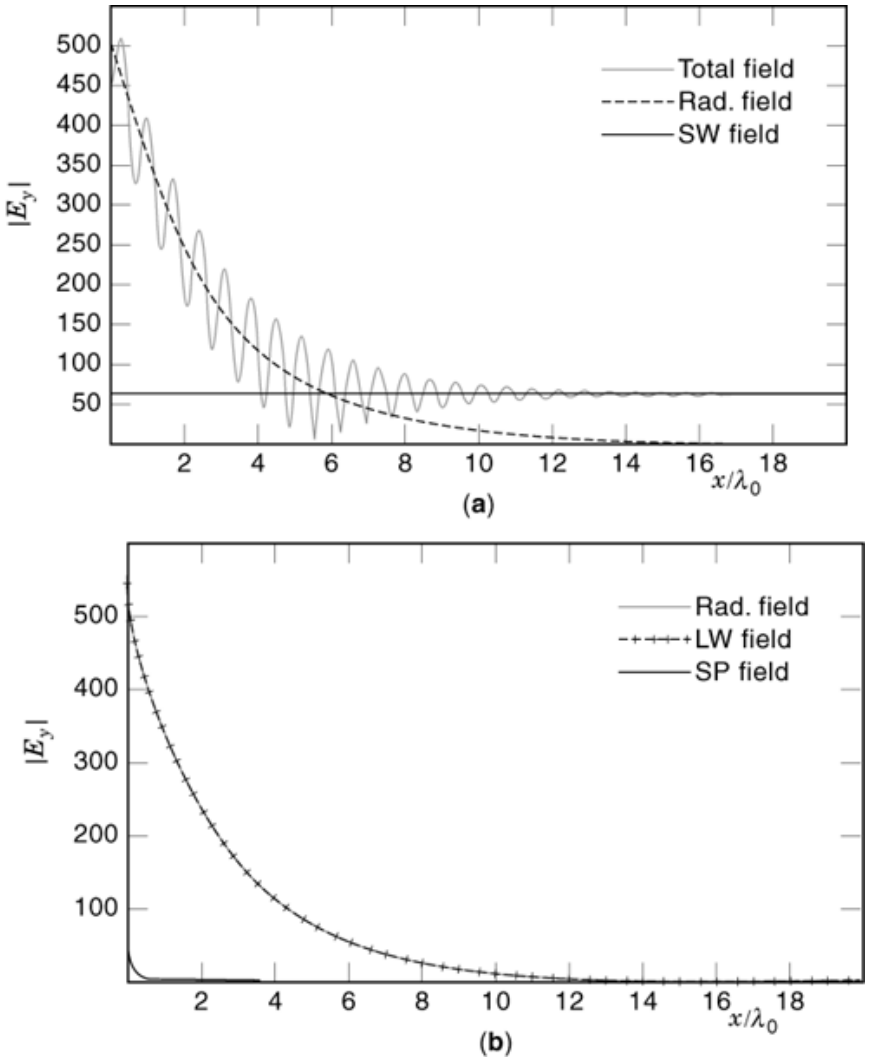

Fig. 13. Components of the aperture field for the two-layer leaky-wave antenna shown in Fig. 12 for a scan angle $\theta_p = 45^\circ$. (a) The total field, radiation field, and surface-wave field is shown. (b) The radiation field, leaky-wave field, and space-wave field is shown.

where

$$E_y^{\text{fin}}(x,0) = \begin{cases} E_y(x,0) & \text{for } |x| < a \\ 0 & \text{for } |x| > a \end{cases} \tag{46}$$

and $k_{x0} = k_0$ in θ. The above integral can be evaluated analytically if Eq. (34) is used and the order of integration is switched so that

$$E_y^{\text{fin}}(\theta) = \frac{\cos\theta}{2\pi} \int_{-\infty}^{\infty} \tilde{G}_E^{yy}(k_x) \int_{-a}^{a} e^{-j(k_x - k_0 \sin\theta)x} dx\, dk_x \tag{47}$$

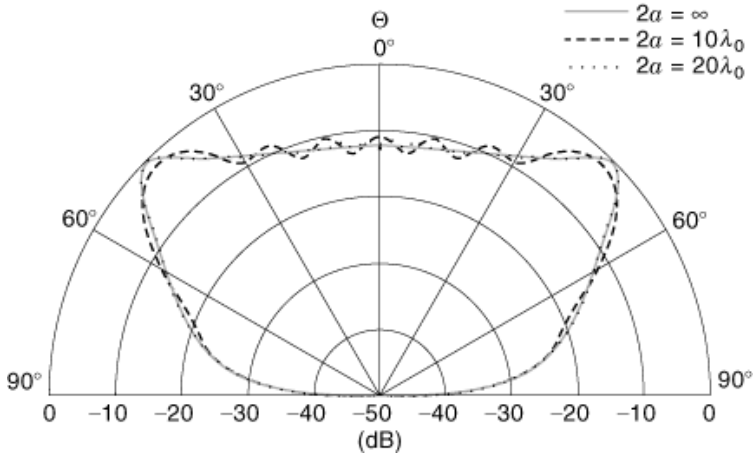

Fig. 14. Far-field pattern of the two-layer antenna of Fig. 12 for an infinite aperture and two finite aperture sizes, $2a = 10\lambda_0$ and $20\lambda_0$. The scan angle is chosen as $\theta_p = 45^\circ$.

Evaluating the inner integral results in the following convolution-type integral,

$$E_y^{\text{fin}}(\theta) = \frac{a\cos\theta}{\pi}\int_{-\infty}^{\infty} \tilde{G}_E^{yy}(k_x)\frac{\sin[(k_x - k_0\sin\theta)a]}{(k_x - k_0\sin\theta)a}dk_x \quad (48)$$

which has to be calculated numerically. Although the integration has been reduced to a single integral, the numerical evaluation can still be time consuming if the pattern is to be calculated at many points. An alternative method for calculating the far-field pattern is to calculate the aperture field numerically first, using the CZT, and then to use the CZT once again to calculate the transform integral in Eq. (45). (An ordinary *FFT* may be used to calculate this transform integral, since the integration is along the real axis. However, the CZT still has the advantage that the sample density for the aperture-field calculation is independent of the sampling density for the pattern calculation, as long as aliasing is avoided.) Calculating the far-field pattern at a large number of far-field angles using the CZT is usually more efficient than directly evaluating the convolution integral in Eq. (48) by Gaussian quadrature, although the degree of improvement is not as large as that seen in the computation of the aperture-field integral in Eq. (34) by the CZT versus direct numerical integration (17).

In Fig. 14 radiation patterns for different aperture diameters 2 a are shown for the structure shown in Fig. 12 with a scan angle of $\theta_p = 45^\circ$. It can be seen that an aperture diameter of approximately 20 wavelengths is sufficient to obtain a smooth pattern.

The normalized far-field radiation patterns produced by the surface-wave and leaky-wave fields can be written in closed form and are given as (assuming a single pole, corresponding to either the surface-wave pole or the TE_2 leaky-wave pole)

$$E_{yp}^{\text{fin}}(\theta) = -j\,\text{Res}\{\tilde{G}_E^{yy}(k_{xp})\}\cos\theta\int_{-a}^{a} e^{-jk_{xp}|x|}e^{jk_0\sin\theta\,x}dx \quad (49)$$

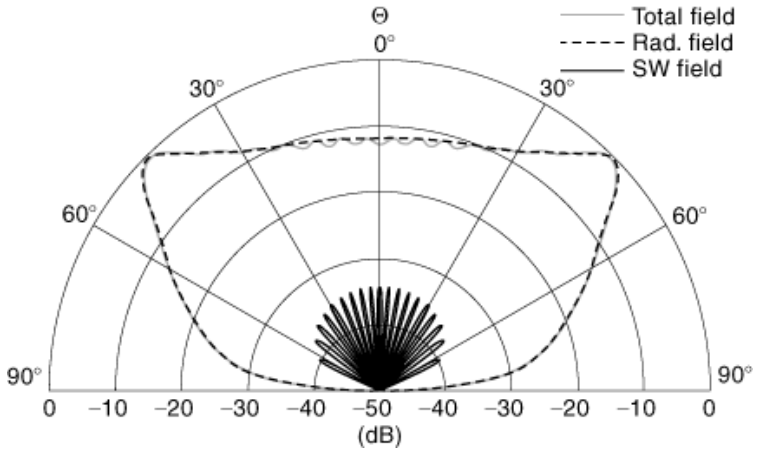

Fig. 15. Far-field radiation patterns due to the total aperture field as well as the radiation and the surface-wave aperture fields for the two-layer antenna of Fig. 12 with $\theta_p = 45^\circ$ and $2a = 20\lambda_0$.

The integral in this expression is, strictly speaking, only convergent when $a = \infty$ for a leaky-wave pole in which the wave field attenuates with distance. However, the case of a surface-wave pole is treated by assuming an infinitesimal amount of loss in the layers, so that the surface wave is slightly attenuated. Dividing the integration into the regions $-a < x < 0$ and $0 < x < a$ and then performing the simple integration yields the normalized far-field pattern of a single surface-wave or leaky-wave field on the aperture as

$$E_{yp}^{\text{fin}}(\theta) = \frac{j2\text{Res}\{\tilde{G}_E^{yy}(k_{xp})\}\cos\theta}{k_{xp}^2 - k_0^2\sin^2\theta} \times \{\underbrace{k_{xp}}_{x=0} - \underbrace{e^{-jk_{xp}a}[k_{xp}\cos(k_0\sin\theta\, a) + jk_0\sin\theta\sin(k_0\sin\theta\, a)]}_{x=\pm a}\} \tag{50}$$

In this equation the contributions from the end points of the integration, namely, $x = 0$ and $x = \pm a$, have been identified. It is interesting to note that the contribution from the aperture edges at $x = \pm a$ vanishes as the aperture size tends to infinity for a leaky mode but not for an unattenuated surface-wave mode. That is, a surface-wave mode will always see the aperture termination and produce a radiation field as a result of this discontinuity. The term arising from $x = 0$ can be viewed physically as another type of discontinuity radiation, arising from the discontinuity in the slope of the aperture field at $x = 0$, due to the presence of the absolute-value sign in the exponent in Eq. (49).

In Fig. 15 the radiation patterns from the different constituent fields that make up the total aperture field are shown for the parameters $\theta_p = 45^\circ$ and $2a = 20\ \lambda_0$. The total field pattern is mainly due to the radiation field on the aperture, as expected. The radiation pattern due to the surface-wave aperture field is fairly negligible, but it is responsible for the ripple observed in the total radiation pattern.

The radiation aperture field is strongly dominated by the leaky-wave aperture field, as can be seen from Fig. 13(b). Hence, the radiation pattern is almost completely due to the leaky-wave aperture field.

If the height h of the line source inside the lower layer is changed, a null in the pattern can be realized at any angle $\theta_n < \theta_p$ if the condition

$$\frac{h}{d_1} = \frac{\sqrt{\epsilon_{r1} - \sin^2\theta_p}}{\sqrt{\epsilon_{r1} - \sin^2\theta_n}} \tag{51}$$

is satisfied. (This condition also applies for a horizontal electric dipole source.) This equation enforces the condition that the source is one-half wavelength above the ground plane with respect to the vertical wavenumber λz in the substrate for radiation at angle $\theta = \theta_n$ in the air region. When $\theta_n = 0^\circ$ is chosen, a null in the pattern is produced at broadside. This may be desirable when producing a scanned beam at angle $\theta_p > 0^\circ$, since the null at broadside will minimize unwanted radiation between the dual beam peaks. The null in the pattern can be viewed as a cancellation between the far fields produced by the radiation field and the surface-wave field on the aperture.

An alternative method for calculating the radiation pattern of the finite-aperture antenna is through the use of the so-called subtraction method (31). In this method the far-field pattern is found by first calculating the pattern for the infinite-aperture case (which can easily be done in closed form) and then subtracting from this the pattern obtained by considering the aperture fields only in the region $|x| > a$ outside the physical aperture. The advantage of this approach is that the aperture field outside the physical aperture can be well approximated by assuming only the surface-wave and dominant leaky-wave fields, that is, neglecting the space-wave field, when the aperture is large (provided that the scan angle is not too close to 90°, since in this case the space-wave aperture field may extend to large distances).

Mathematically, the normalized far-field pattern for the finite-aperture leaky-wave antenna is approximated as

$$E_y^{\text{fin}}(\theta) = E_y^{\infty}(\theta) - E_{yp}^{a,\infty\text{LW}}(\theta) - E_{yp}^{a,\infty\text{SW}}(\theta) \tag{52}$$

where $E_y{}^{\infty}(\theta)$ is the radiation pattern from the infinite structure, $E^{a,\infty\text{LW}}{}_{yp}(\theta)$ is the pattern due to the aperture field of the leaky wave outside the physical aperture (i.e., $|x| > a$), and $E^{\text{a},\infty\text{SW}}{}_{yp}\ (\theta)$ is the pattern due to the aperture field of the surface wave outside the physical aperture. The radiation pattern for the infinite-aperture case is given in closed form as

$$E_y^{\infty}(\theta) = \cos\theta\ \tilde{G}_E^{yy}(k_0 \sin\ \theta) \tag{53}$$

The far-field pattern of the leaky-wave aperture field outside the physical aperture is given by

$$E_{yp}^{\text{a},\infty\text{LW}}(\theta) = \frac{j2\,\text{Res}\{\tilde{G}_E^{yy}(k_{xp})\}\cos\theta}{k_{xp}^2 - k_0^2\sin^2\theta} \times\{e^{-jk_{xp}a}[k_{xp}\cos(k_0\sin\theta\, a) + jk_0\sin\theta\sin(k_0\sin\theta\, a)]\} \tag{54}$$

The far-field pattern of the surface-wave field outside the physical aperture is given by the same formula, with k_{xp} denoting the propagation wave number of the surface-wave mode. If more than one leaky wave or

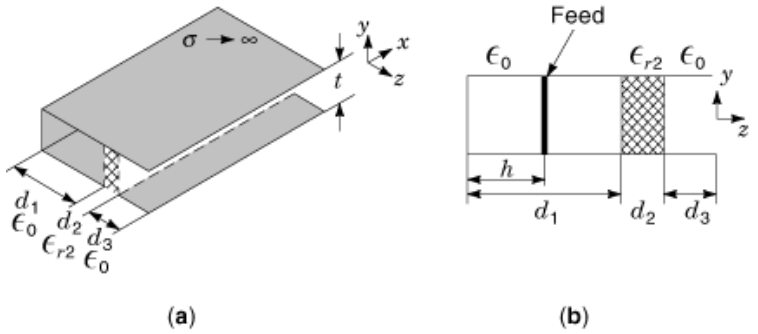

Fig. 16. Geometry of the dielectric parallel-plate leaky-wave antenna: (a) full view; (b) cross section.

surface wave is included, the formula for the pattern calculation becomes

$$E_y^{\text{fin}}(\theta) = E_y^{\infty}(\theta) - \sum_p E_{yp}^{a,\infty\text{LW}}(\theta) - \sum_q E_{yq}^{a,\infty\text{SW}}(\theta) \qquad (55)$$

For the one-dimensional two-layer structure, one dominant leaky mode (the TE_2 mode) and one surface-wave mode (the TE_1 mode) is sufficient.

A Dielectric Parallel-Plate Leaky-Wave Antenna. As a practical example of the one-dimensional leaky-wave antenna, we introduce a structure that radiates either a broadside beam or a bidirectional beam. The principle configuration is shown in Fig. 16. The parallel plates create a field inside the structure that is uniform in the y direction (at least for points not too close to the radiating aperture) so that the one-dimensional analysis of this section is applicable. The metal plates are extended a distance d_3 above the superstrate, creating a baffle region. This baffle region allows for the higher-order parallel-plate modes created at the aperture discontinuity to decay before reaching the superstrate. For given plate separation t, the distance d_3 can easily be determined so that the higher modes are sufficiently attenuated. This allows the analysis of the present section to be used for the analysis of this structure. The baffle region also gives an additional degree of design flexibility, since the attenuation of the leaky mode can be controlled to some extent by varying the baffle height d_3. More details about the effects of the baffle height can be found in Ref. 38

The feed can be practically realized by a simple coaxial connector, where the outer conductor is connected to one plate and the inner conductor of the coaxial connector is extended through the structure and connected to the opposite plate. The feed is located lengthwise at the middle of the structure in order to allow for the excitation of a bidirectional leaky wave.

If a unidirectional scanned beam is preferred, the structure can be fed at a distance of one-quarter guide wavelength from one end of the structure, and the corresponding end closed off by a shorting metal plate. This will allow for the excitation of a leaky wave that travels in only one direction along the length of the structure. In this case the excitation of the structure can be viewed as coming from the original feed plus an image current (which is 180° out of phase). The analysis developed here for a single feed can be directly extended to account for the two feeds, although this is not discussed any further here.

Alternatively, a unidirectional beam can be produced by feeding the structure in Fig. 16 with a rectangular waveguide. Instead of using a coaxial cable, a waveguide having dimensions that match those of the substrate is ud. The analysis developed in this section can be directly modified to account for the end feed, although the details are omitted here.

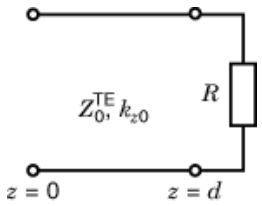

Fig. 17. Equivalent-circuit model for the parallel-plate to free-space transition at the top of the baffle for the structure in Fig. 16.

The electric field inside the dielectric parallel-plate waveguide is similar to the field inside the infinite two-layer structure of Fig. 12 excited by an infinite electric line source. Differences occur at the transition from the waveguide to free space. An equivalent-circuit representation for the parallel-plate to free-space discontinuity is available in the literature (39). This equivalent circuit, shown in Fig. 17, consists of an extension of transmission line of length d beyond the physical termination of the aperture, along with a resistive termination R at the end of the extended line. The extended transmission line has the same characteristic impedance $Z^{\mathrm{TE}}{}_0$ as the lines that model regions 1 and 3.

The distance d and the resistance R can be found in Ref. 25 The extension distance d is given as a function of k_x as

$$k_{z0}d = x \ln \frac{2e}{\gamma x} - S_1(x; 0, 0) \tag{56}$$

with

$$S_1(x; 0, 0) = \sum_{n=1}^{\infty} \left(\arcsin \frac{x}{n} - \frac{x}{n} \right) \tag{57}$$

$$x = k_{z0} \frac{t}{2\pi} \tag{58}$$

The two constants e and γ are the usual natural-log base and Euler's constant, respectively, given by $e = 2.718$ and $\gamma = 1.781$. The resistance R is given by

$$\frac{R}{Z_0^{\mathrm{TE}}} = \coth \frac{\pi x}{2} \tag{59}$$

for $|x| < 1$.

In the calculation of the aperture fields and the far-field pattern for the parallel-plate leaky-wave antenna, the analysis developed previously for the two-layer structure in Fig. 12 may be used with only minor modification. The spectral-domain Green's function in Eq. (34) is modified to account for the aperture termination by simply adding the equivalent circuit in Fig. 17 to the end of the transmission-line model. The rest of the analysis remains unchanged.

For an experimental design the following parameters have been chosen. Layer 2 is realized by a PTFE (teflon) ($\varepsilon_{r2} = 2.45$) slab with a thickness $d_2 = 4.44$ mm. Media 1 and 3 are air, having thickness $d_1 = 17.52$

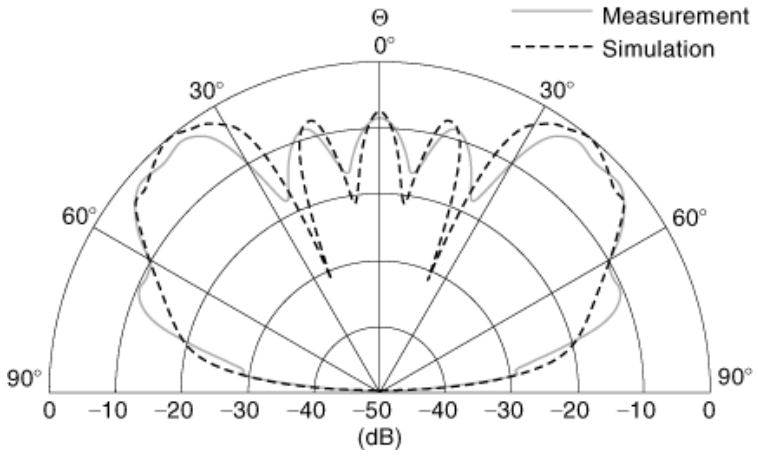

Fig. 18. Measured (—) and calculated (—) radiation patterns for a dielectric parallel-plate leaky-wave antenna with a bidirectional beam, fed by a coaxial probe at the center of the structure. The frequency is 12.1 GHz and the desired scan angle is $\theta_p = 45^\circ$. The superstrate has $\epsilon_{r2} = 2.45$. $d_1 = 17.52$ mm, $d_2 = 4.44$ mm, $d_3 = 24.8$ mm, $h_1/d_1 = 0.37$.

mm and $d_3 = 24.8$ mm, respectively. The design frequency is 12.1 GHz, and the desired scan angle is $\theta_p = 45^\circ$. The aperture size is $2a = 192$ mm. The source inside the lower layer is located at $h/d_1 = 0.37$. A comparison between measurement and simulation is shown in Fig. 18. The beamwidth of the main beam and sidelobes is predicted fairly well, although there is a slight shift in the location of the peaks. This could possibly be due to the nonideal absorber used or tolerance errors in the substrate thickness, which would cause an error in the phase constant of the leaky mode.

As mentioned, a unidirectional beam can be produced by using a rectangular waveguide feed at the end of the structure. Instead of using a coaxial cable feed at the center of the structure, a rectangular waveguide having dimensions that match those of the (air) substrate is used. The waveguide mode essentially turns into a leaky mode after the mode enters into the parallel-plate antenna region, in this case. To demonstrate the practicality of this type of feed an experimental antenna was built. The design frequency was 36.8 GHz and the layer thicknesses were chosen as $d_1 = 5.75$ mm for the lower layer and $d_2 = 0.635$ mm for the upper (superstrate) layer, giving a scan angle $\theta_p = 45^\circ$. The dielectric constants were $\varepsilon_{r2} = 10.8$ and $\varepsilon_{r1} = 1.0$. The stub height d_3 was chosen as 6.7 mm. The parallel-plate separation was $t = 3.1$ mm. A comparison between measured and calculated results is shown in Fig. 19. The calculated result was obtained in this case by Fourier transforming the aperture field of the dominant leaky mode only. The agreement between the calculated and measured patterns is good for the main beam except for a slight beam shift, which could be caused by tolerance errors in the substrate thickness or a slight alignment error in the measurements. The error in the sidelobes could be due to the approximation of the aperture field by the leaky-mode field or the ideal absorber assumption used in the calculations.

Analysis of Two-Dimensional Dielectric Leaky-Wave Antennas

In the previous section, one-dimensional dielectric leaky-wave antenna structures were investigated. The study of the one-dimensional structure is important because many of the fundamental antenna properties are revealed by an investigation of this simpler structure. Furthermore, a practical parallel-plate leaky-wave antenna based on the one-dimensional structure was realized. This antenna was capable of producing either

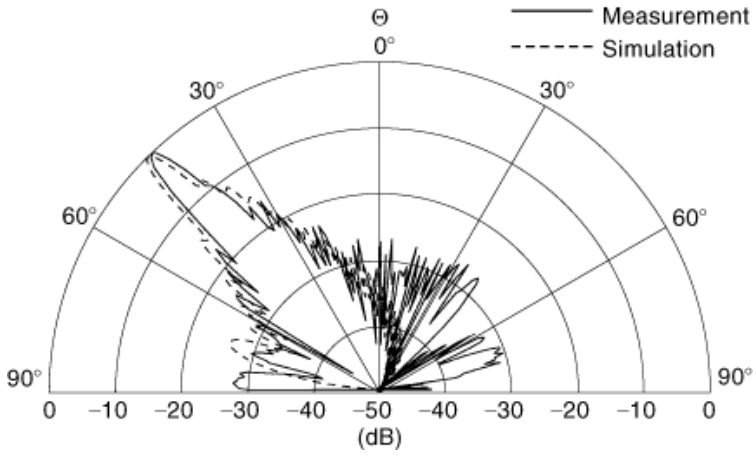

Fig. 19. Measured (—) and calculated (—) radiation patterns for a dielectric parallel-plate antenna with a unidirectional beam, fed by a rectangular waveguide. The frequency is 36.8 GHz and the desired scan angle is $\theta_p = 45^\circ$. The superstrate has $\epsilon_{r2} = 10.8$. $d_1 = 5.75$ mm, $d_2 = 0.635$ mm, $d_3 = 6.7$ mm, $t = 3.1$ mm.

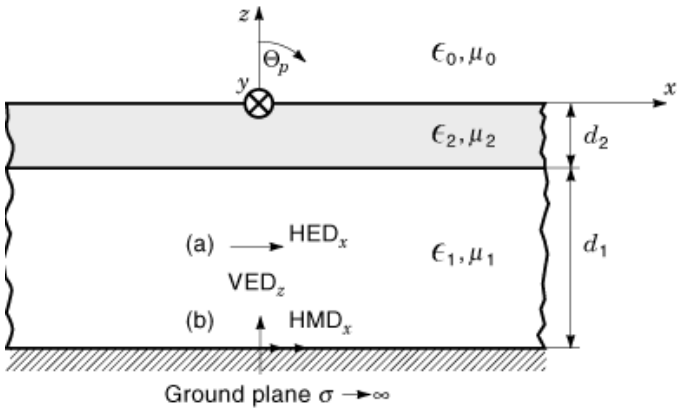

Fig. 20. Geometry of the two-dimensional dielectric leaky-wave antenna, consisting of two dielectric layers above a ground plane, excited by an *HED*, *HMD*, or *VED* source. This antenna provides a narrow-beam pattern about any desired scan angle θ_p.

a broadside beam or a scanned beam (unidirectional or bidirectional) in one plane (the *H* plane). The *E*-plane pattern of this type of antenna will usually be quite broad, due to the narrow dimension of the antenna (the thickness t in Fig. 16). That is, a "fan" beam is produced from this type of antenna. A two-dimensional leaky-wave antenna can be used to produce a narrow pencil beam at broadside or a conical beam at a scan angle θ_p, which may be more desirable for many applications. The calculation of the aperture field and the far-field radiation pattern from a two-dimensional leaky-wave antenna structure is the subject of this section. The basic structure considered here in shown in Fig. 20. The antenna consists of two dielectric layers above a ground plane, excited by a dipole source. (More than two layers can be used to produce a more directive antenna, as Fig. 1 shows. Results will only be shown for the two-layer structure of Fig. 20, however.) To achieve maximum radiated power, a horizontal electric dipole (*HED*) source should be placed in the middle of the lower layer,

whereas a horizontal magnetic dipole (*HMD*) or vertical electric dipole (*VED*) source should be placed at the ground plane.

The layers act as a guiding structure for the radiating leaky wave fields, which propagate radially outward from the dipole source. Unlike the one-dimensional case, the dipole source excites both TE and TM dominant leaky modes. For the two-layer structure, the dominant leaky modes are the TE_2 and TM_2 modes, as discussed previously. The *HED* or *HMD* dipole sources can be used to produce either a broadside beam or a scanned conical beam. A vertical dipole source, such as the *VED*, can only be used to produce a scanned beam, since the dipole pattern itself has a null at broadside. From another point of view, the vertical dipole source will only excite one type of cylindrical leaky wave (TM for the *VED* source), whereas both a TM and a TE leaky mode are required to produce a broadside beam (18), as discussed earlier. For all three types of sources (*HED*, *HMD*, *VED*) the corresponding formulas for calculating the tangential aperture fields as well as the far-field radiation pattern will be given. The behavior of the different wave types (surface wave, leaky wave, and space wave) is similar to the behavior of the waves on the one-dimensional antenna structure and will not be considered.

If very small sources (such as point dipoles) are assumed, the necessary two-dimensional Fourier transform appearing in the spectral-domain calculation of the aperture fields can be replaced by a one-dimensional Hankel transform (40). Most of the formulas presented here can be found in Ref. 15, along with a complete derivation. Therefore, only the results will be presented here for brevity.

Aperture Field. For the horizontal electric dipole in the x direction, the tangential fields on the aperture ($z = 0$) can be calculated using

$$E_\rho(\rho, \varphi, 0) = \frac{-1}{2\pi}\cos\varphi \int_0^\infty \left(V_i^{\mathrm{TM}}(k_\mathrm{t}) J_1'(k_\mathrm{t}\rho) + V_i^{\mathrm{TE}}(k_\mathrm{t}) \frac{J_1(k_\mathrm{t}\rho)}{k_\mathrm{t}\rho} \right) k_\mathrm{t}\, dk_\mathrm{t} \tag{60a}$$

$$E_\varphi(\rho, \varphi, 0) = \frac{1}{2\pi}\sin\varphi \int_0^\infty \left(V_i^{\mathrm{TM}}(k_\mathrm{t}) \frac{J_1(k_\mathrm{t}\rho)}{k_\mathrm{t}\rho} + V_i^{\mathrm{TE}}(k_\mathrm{t}) J_1'(k_\mathrm{t}\rho) \right) k_\mathrm{t}\, dk_\mathrm{t} \tag{60b}$$

In these equations the two-dimensional inverse Fourier transform integral has been reduced to a single integration in the spectral radial variable k_t by analytically integrating in the spectral angle variable in polar coordinates.

As in the one-dimensional case, the aperture field can be decomposed into surface-wave, leaky-wave, and space-wave fields. To do this, the integrations are first extended to $(-\infty, \infty)$ by using the four identities

$$J_1(x) = \frac{1}{2}\left[H_1^{(1)}(x) + H_1^{(2)}(x) \right]$$

and

$$H_1^{(1)}(x) = H_1^{(2)}(-x)$$

$$J_1'(x) = \tfrac{1}{2}\left[H_1^{(1)'}(x) + H_1^{(2)'}(x) \right]$$

The aperture-field equations then become

$$E_\rho(\rho,\varphi,0) = \frac{-1}{4\pi}\cos\varphi\int_{-\infty}^{\infty}\left(V_i^{\mathrm{TM}}(k_t)H_1^{(2)'}(k_t\rho)+V_i^{\mathrm{TE}}(k_t)\frac{H_1^{(2)}(k_t\rho)}{k_t\rho}\right)k_t\,dk_t \tag{61a}$$

$$E_\varphi(\rho,\varphi,0) = \frac{1}{4\pi}\sin\varphi\int_{-\infty}^{\infty}\left\{V_i^{\mathrm{TM}}(k_t)\frac{H_1^{(2)}(k_t\rho)}{k_t\rho}+V_i^{\mathrm{TE}}(k_t)H_1^{(2)'}(k_t\rho)\right\}k_t\,dk_t \tag{61b}$$

The integration is then along the same path as shown in Fig. 4. Using the asymptotic form of the Hankel functions and the steepest-descent transformation, Eq. (30a), allows the path to be deformed into the same ESDP path shown in Fig. 5. The decomposition of the total aperture field into its constituent parts (surface-wave, leaky-wave, and space-wave fields) is then done in the same manner as was discussed for the one-dimensional case in the previous section. As for the one- dimensional case, it is convenient to incorporate the same transition function into the definition of the leaky-wave and space-wave aperture fields, so that these fields remain continuous as the leaky-wave pole crosses the ESDP path. This has been done in the results presented in the following.

For a two-layer structure with parameters $\epsilon_{r1} = 2.1$, $\epsilon_{r2} = 10.8$, and a scan angle $\theta_p = 45^\circ$, both tangential electric field components $E_\rho(\rho, 0, 0)$ and $E_\varphi(\rho, \pi/2, 0)$ are shown in Fig. 21. The total field, radiation (continuous-spectrum) field, and surface-wave field on the aperture are shown in Figs. 21(a) and 21(b), whereas the radiation field, leaky-wave field, and space-wave field on the aperture are shown in Figs. 21(c) and 21(d).

In contrast to the one-dimensional antenna, where the surface-wave field did not decay with distance, the surface waves in the two-dimensional case decay as $1/\sqrt{\rho}$ in the lossless case. As mentioned previously, the attenuation constant of the TE_2 leaky mode is smaller than that of the TM_2 leaky mode. In this example the TE_2 leaky mode has a propagation wavenumber $k_t/k_0 = 0.717 - j\,0.059$ whereas the wave number for the TM_2 mode is $k_t/k_0 = 0.695 - j\,0.137$. The TE_2 mode is mainly responsible for the E_φ field component on the aperture, and the TM_2 mode is mainly responsible for the E_ρ component. Hence, the leaky-wave aperture field decays more slowly for the E_φ field component than for the E_ρ component. This behavior is clearly seen in Figs. 21(c) and 21(d). It is also clear from these figures that the radiation aperture field is dominated by the leaky waves. As mentioned earlier, this will normally be the case unless the scan angle becomes close to 90°, in which case the narrow-beam pattern is due primarily to the space-wave aperture field and not the leaky-wave aperture field. Very large apertures are required to realize narrow-beam patterns for such large scan angles, because the space wave does not decay exponentially.

Practically, an *HED* source can be realized by using a bent coaxial monopole, or by using a printed dipole that is electromagnetically (proximity) coupled to a feed line.

For a horizontal magnetic dipole source, the aperture fields can be calculated from the following equations:

$$E_\rho(\rho,\varphi,0) = \frac{1}{4\pi}\sin\varphi\int_{-\infty}^{\infty}\left(V_v^{\mathrm{TM}}(k_t)H_1^{(2)'}(k_t\rho)+V_v^{\mathrm{TE}}(k_t)\frac{H_1^{(2)}(k_t\rho)}{k_t\rho}\right)k_t\,dk_t \tag{62a}$$

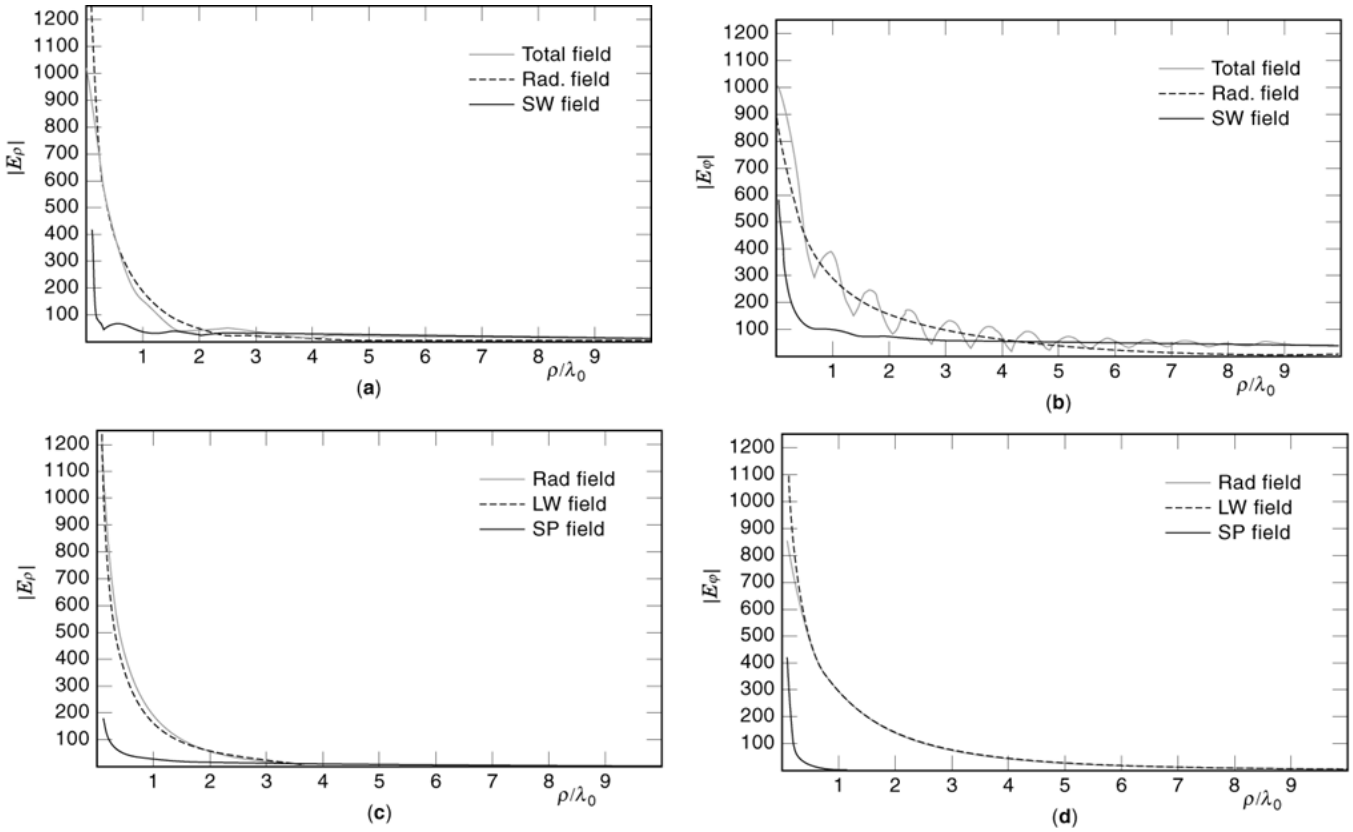

Fig. 21. (a) $E_\rho(\rho, 0, 0)$ component and (b) $E_\varphi(\rho, \pi/2, 0)$ component of the total field, radiation field, and surface-wave field on the aperture. (c) $E_\rho(\rho, 0, 0)$ component and (d) $E_\varphi(\rho, \pi/2, 0)$ component of the radiation field, leaky-wave field, and space-wave field on the aperture. All components are for the two-layer dielectric leaky-wave antenna with a scan angle of $\theta_p = 45^\circ$. The exciting HED_z source is located in the middle of the lower layer. $\varepsilon_{r1} = 2.1$, $\varepsilon_{r2} = 10.8$.

$$E_\varphi(\rho, \varphi, 0) = \frac{1}{4\pi}\cos\varphi \int_{-\infty}^{\infty} \left(V_v^{\text{TM}}(k_t)\frac{H_1^{(2)}(k_t\rho)}{k_t\rho} + V_v^{\text{TE}}(k_t)H_1^{(2)\prime}(k_t\rho) \right) k_t\, dk_t \tag{62b}$$

This type of source can be easily realized using a waveguide aperture or slot feed at the ground plane, which is modeled as a magnetic current.

Finally, the tangential aperture field for a vertical electric dipole source can be written as

$$E_\rho(\rho, \varphi, 0) = \frac{\omega\varepsilon_0\varepsilon_{r1}\eta_0^2}{4\pi j k_0^2} \int_{-\infty}^{\infty} V_v^{\text{TM}}(k_t)H_1^{(2)}(k_t\rho)k_t^2\, dk_t \tag{63a}$$

$$E_\varphi(\rho, \varphi, 0) = 0 \tag{63b}$$

As with the HMD source, the VED has to be placed on the ground plane, as indicated in Fig. 20, to achieve maximum radiated power. A practical realization of such a feed may be easily obtained using a coaxial feed at the ground plane. The *VED* source excites only TM waves, which, due to the circular symmetry, have nφ variation. As mentioned previously, this type of aperture field can only produce a scanned beam since there will always be a null in the radiation pattern at broadside.

Far-Field Analysis. As described in Ref. 15, the far-field pattern of a circularly symmetric aperture of radius a, excited by a dipole source at $\rho = 0$ and terminated at $\rho = a$ with ideal absorber can be calculated by integrating over the aperture field in cylindrical coordinates. Both the integration in ρ and in φ can be performed analytically, so that the far-field pattern is given by a single integration in the spectral variable k_t. For the HED_z source, the result is

$$E_\theta(r,\theta,\varphi) = -R(r)\cos\varphi\int_{-\infty}^{\infty}\left[V_i^{\mathrm{TM}}(k_t)P_1(k_t,\theta)+V_i^{TE}(k_t)C(k_t,\theta)\right]k_t\,dk_t \tag{64a}$$

$$E_\varphi(r,\theta,\varphi) = R(r)\sin\varphi\cos\theta\int_{-\infty}^{\infty}\left[V_i^{\mathrm{TM}}(k_t)C(k_t,\theta)+V_i^{\mathrm{TE}}(k_t)\mathrm{P}_1(k_t,\theta)\right]k_t\,dk_t \tag{64b}$$

where the functions

$$P_1(k_t,\theta) = \frac{k_t a H_1^{(2)}(k_t a)J_0(\xi a)-\xi a H_0^{(2)}(k_t a)J_1(\xi a)}{k_t^2-\xi^2} - \frac{2j/\pi}{k_t^2-\xi^2} - C(\theta,k_t) \tag{64c}$$

$$C(k_t,\theta) = \frac{H_1^{(2)}(k_t a)J_1(\xi a)}{k_t\xi} - \frac{j\xi/(\pi k_t)}{k_t\xi} \tag{64d}$$

and

$$R(r) = \frac{jk_0}{4\pi r}e^{-jk_0 r} \tag{64e}$$

have been defined. The far-field radiation pattern produced by an HMD_x source is

$$E_\theta(r,\theta,\varphi) = R(r)\sin\varphi\int_{-\infty}^{\infty}\left[V_v^{\mathrm{TM}}(k_t)P_1(k_t,\theta)+V_v^{\mathrm{TE}}(k_t)C(k_t,\theta)\right]k_t dk_t \tag{65a}$$

$$E_\varphi(r,\theta,\varphi) = R(r)\cos\varphi\cos\theta\int_{-\infty}^{\infty}\left[V_v^{\mathrm{TM}}(k_t)\mathrm{C}(k_t,\theta)+V_v^{\mathrm{TE}}(k_t)\mathrm{P}_1(k_t,\theta)\right]k_t dk_t \tag{65b}$$

Finally, the far-field pattern of the VED source is

$$E_\theta(r,\theta) = R(r)\left(\frac{-\eta_0}{k_0\epsilon_r}\right)\int_{-\infty}^{\infty} V_v^{\mathrm{TM}}(k_t)P_0(k_t,\theta)k_t^2\,dk_t \qquad (66a)$$

where

$$P_0(k_t,\theta) = \frac{\xi a H_1^{(2)}(k_t a)\cdot J_0(\xi a) - k_t a H_0^{(2)}(k_t a)\cdot J_1(\xi a)}{k_t^2 - \xi^2} \qquad (66b)$$

and $\eta_0 = \sqrt{\mu_0/\epsilon_0}$. The radiation pattern of the VED source at the center of the circular aperture is polarized entirely in the θ direction and is independent of φ

In Fig. 22 the E_θ and the E_φ components of the far-field pattern for the two-layer structure having $\epsilon_{r1} = 2.1$, $\epsilon_{r2} = 10.8$, and a scan angle $\theta_p = 45^\circ$ are shown for two different aperture radii, $a = 5\ \lambda_0$ and $10\lambda_0$, along with the pattern for an infinite aperture ($a = \infty$). The source is an HED_z dipole in the middle of the lower layer. In both planes the influence of the aperture size on the radiation pattern is clearly visible. The influence of the aperture size is more pronounced in the E_θ pattern at $\varphi = 0$, due to the fact that the dominant TM_θ surface wave is launched the strongest in the $\varphi = 0$ direction, and weakest in the $\varphi = \pi/2$ direction.

The far-field pattern can be decomposed into a pattern coming from the radiation (continuous-spectrum) field on the aperture, and one coming from the surface-wave fields on the aperture. The surface-wave radiation pattern can be found by evaluating the residue contribution of the integrals, Eqs. (64a) to (66a), at the surface-wave poles. Alternatively, the far-field pattern due to the aperture radiation field can be first found by integrating along the path C_2 shown in Fig. 11, and then the surface-wave radiation pattern can be found by subtracting the pattern due to the radiation aperture field from the total far-field pattern. For the present structure, the TM_0, TE_1, and TM_1 modes are surface-wave modes, and are all excited by an HED_x dipole source and thus contribute to the surface-wave radiation pattern.

Figure 23(a) shows the total E plane ($\varphi = 0^\circ$) far-field pattern and the far-field patterns due to the aperture radiation field and the surface-wave fields, for the same two-layer structure used in Fig. 22. As can be seen, the pattern due to the radiation aperture field dominates the surface-wave contribution. However, the surface-wave pattern is responsible for the ripples seen in the total pattern. The H plane ($\varphi = 90^\circ$) pattern shown in Fig. 23(b) exhibits much less surface-wave radiation than does the E-plane pattern, especially near the horizon ($\theta = 90^\circ$). This is due to the fact that the TM_0 surface wave is primarily excited in the E -plane direction.

As in the one-dimensional case, the far-field pattern due to the radiation field on the aperture can be decomposed into a pattern due to the leaky-wave aperture field and one due to the space-wave aperture field. These radiation patterns are shown in Fig. 23(c) for the E plane and in Fig. 23(d) for the H plane for the same structure as in Figs. 23(a) and 23(b). The leaky-wave radiation pattern is calculated from the residue contribution to Eqs. (64a) to (66a) at the dominant leaky-wave poles (TM_2 and TE_2 poles), accounting for the transition function as discussed in the previous section. The space-wave radiation pattern is the pattern due to the radiation (continuous-spectrum) field on the aperture minus the pattern due to the leaky-wa aperture field.

From Figs. 23(c) and 23(d), it is seen that the leaky-wave aperture field dominates the calculation of the far-field pattern. This is especially true in the H plane, where the space-wave radiation pattern is fairly weak. In the E plane, the space-wave radiation pattern is significantly stronger, especially near the horizon.

In addition to using a symmetric circular aperture terminated with ideal absorber, a rectangular aperture can also be used. In this case the calculation of the far-field pattern cannot be reduced to a single integration as for the circular case. By expanding the fields inside the rectangular aperture into a Fourier series in φ' with coefficients that are dependent on the radius ρ', it is possible to perform the φ' integration analytically so that

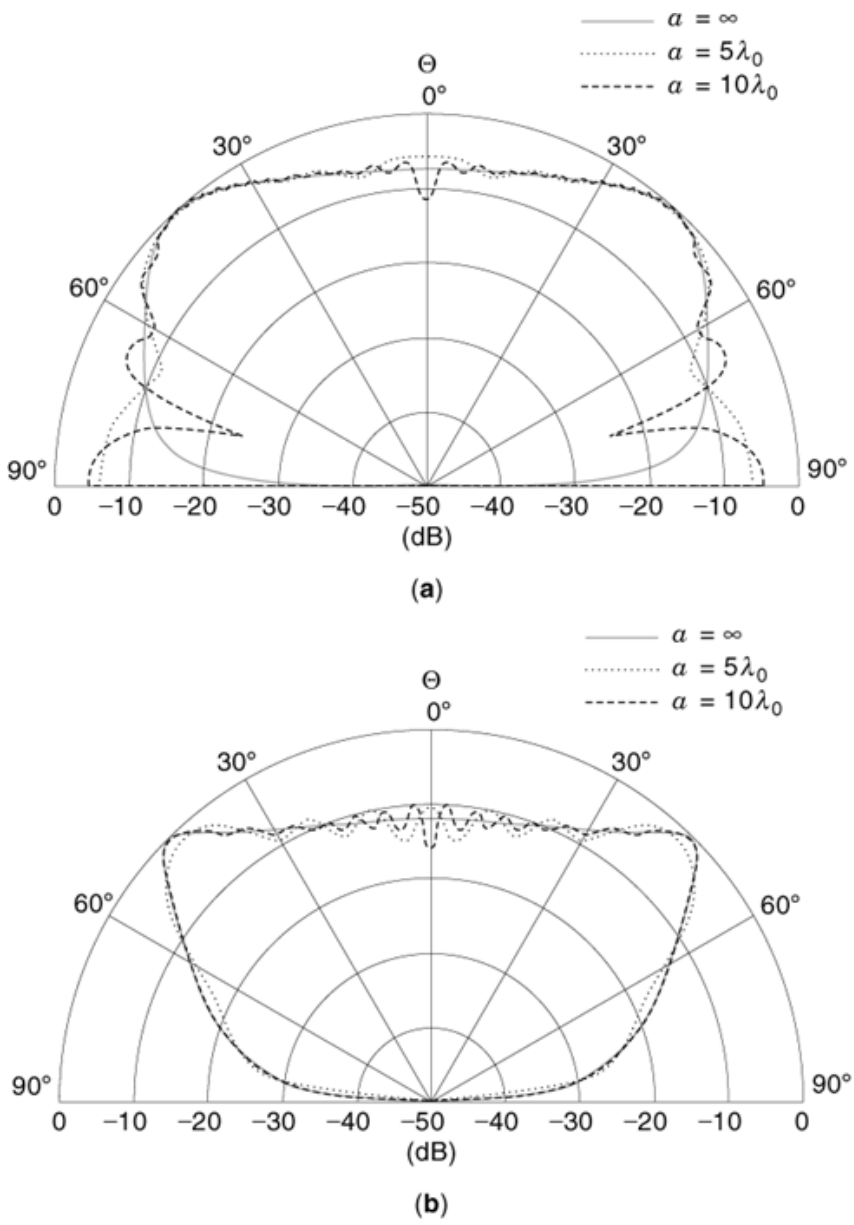

Fig. 22. Far-field pattern (a) $E_\theta(r, \theta, 0)$ and (b) $E_{\text{phiv;}}(r, \theta, \pi/2)$ for the two-layer dielectric leaky-wave antenna having a scan angle $\theta_p = 45^\circ$. Results are shown for an aperture radius $a = 5\lambda_0$, $10\lambda_0$, and ∞. The exciting *HED* source is located in the middle of the lower layer. $\varepsilon_{r1} = 2.1$, $\varepsilon_{r2} = 10.8$.

the resulting expressions for the far-field components involve an integration in k_t and ρ' for each term of the series. More details can be found in Ref. 15.

The calculation of the radiation pattern using the preceding equations will give an exact result under the assumption of an ideal absorber terminating the finite-radius aperture. The calculation time for a large number of angles may begin to become large, however. For scan angles that are not too close to 90°, the calculation

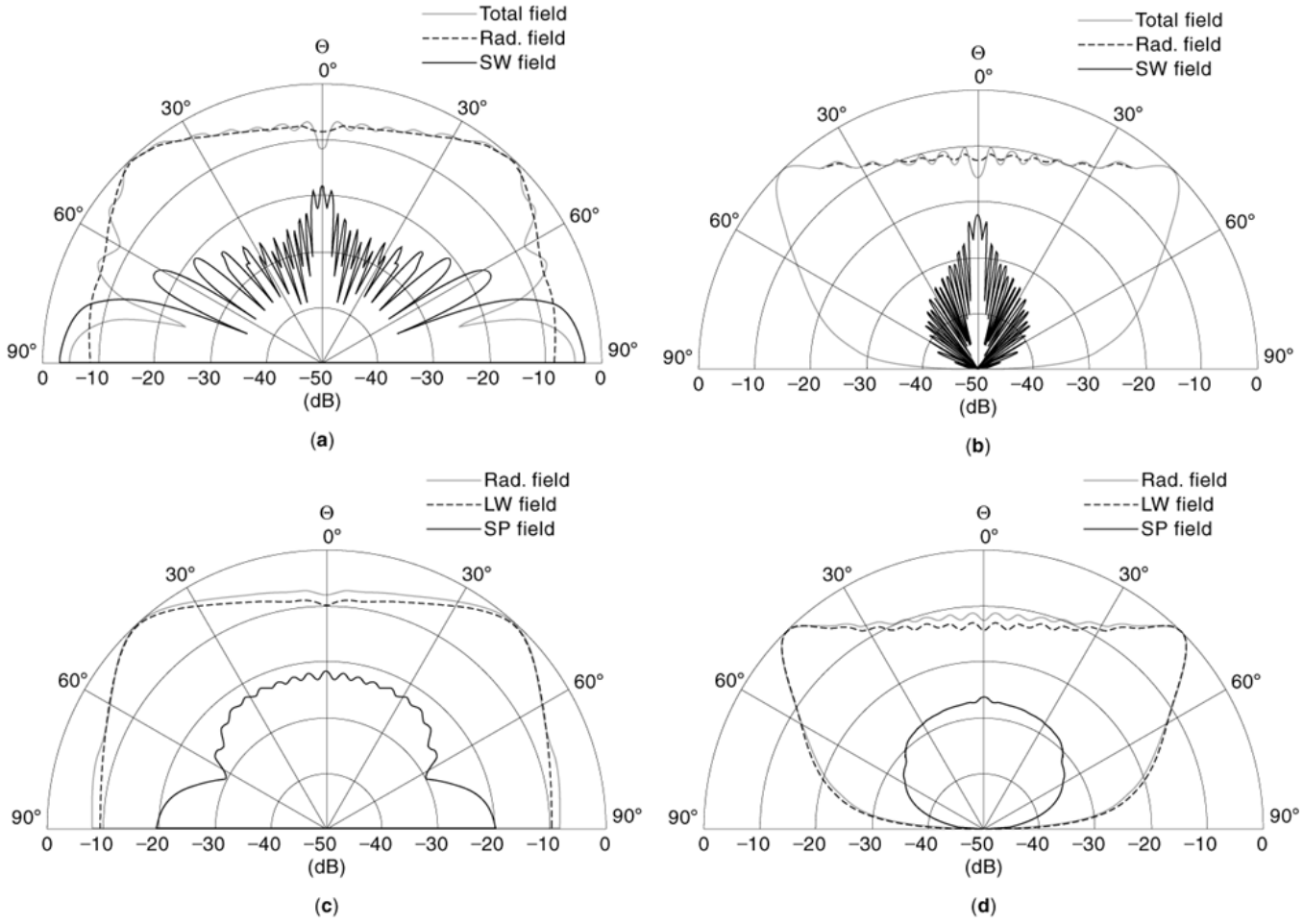

Fig. 23. (a) E-plane ($\varphi = 0$) and (b) H-plane ($\varphi = \pi/2$) far-field pattern due to the total aperture field, the radiation aperture field, and the surface-wave aperture field. (c) E-plane ($\varphi = 0$) and (d) H-plane ($\varphi = \pi/2$) far-field pattern due to the radiation aperture field, the leaky-wave aperture field, and the space-wave aperture field. All patterns are for the two-layer dielectric leaky-wave antenna with an aperture size $a = 10\lambda_0$ and a scan angle $\theta_p = 45^\circ$. The exciting HED_z source is located in the middle of the lower layer. $\varepsilon_{r1} = 2.1$, $\varepsilon_{r2} = 10.8$.

time can be improved significantly by using the subtraction method, which was discussed previously for the one-dimensional case. The subtraction method starts with the pattern for the infinite aperture case, which may be easily calculated in closed form by reciprocity (12). The patterns due to the leaky-wave and surface-wave fields exterior to the physical aperture (i.e., the fields in the region $\rho > a$) are then subtracted from the infinite-aperture pattern to yield the pattern of the finite-aperture antenna terminated with an ideal absorber. Mathematically, the far-field radiation pattern is represented as

$$E_\theta^{\text{fin}} = E_\theta^{\infty} - \sum_p E_{\theta p}^{a,\infty\,\text{LW}} - \sum_q E_{\theta q}^{a,\infty\,\text{SW}} \qquad (67a)$$

$$E_\varphi^{\text{fin}} = E_\varphi^{\infty} - \sum_p E_{\varphi p}^{a,\infty\,\text{LW}} - \sum_q E_{\varphi q}^{a,\infty\,\text{SW}} \qquad (67b)$$

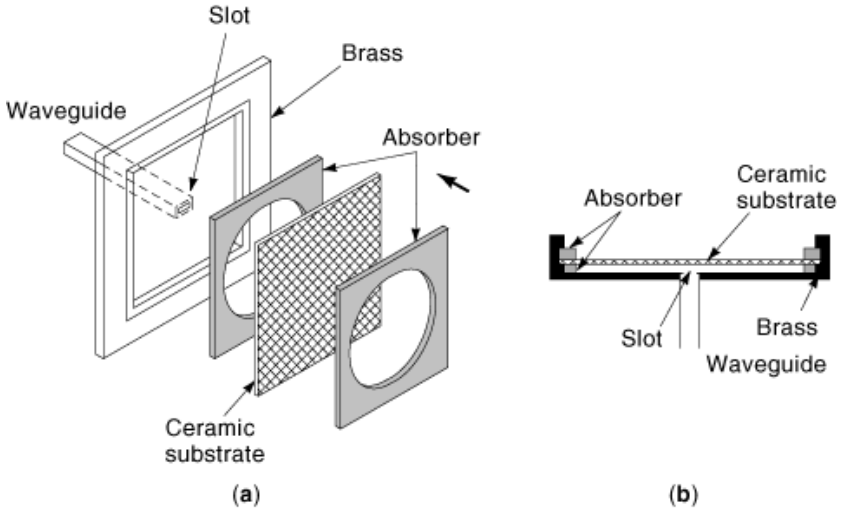

Fig. 24. Practical implementation of the two-layer dielectric leaky-wave antenna structure, excited from a waveguide: (a) isometric view; (b) cross section. $\varepsilon_{r1} = 1.0$, $d_1 = 2.4$ mm, $\varepsilon_{r2} = 55$, $d_2 = 0.5$ mm.

The subtraction method was discussed in Ref. 31 for two-dimensional structures with circular apertures. (In Ref. 31 only the pattern due to the exterior leaky-wave fields was subtracted and not the pattern due to the exterior surface-wave fields. Subtracting the exterior surface-wave fields, as discussed previously for the one-dimensional case, can improve the accuracy.) Results comparing the exact pattern with that obtained by the subtraction method are presented in Ref. 15. As for the one-dimensional case, the subtraction method gives accurate results as long as the scan angle does not approach 90°. For scan angles near the horizon the subtraction method loses accuracy as discussed earlier.

Measurements. To verify the calculations, two different dielectric leaky-wave antenna structures were built, based on the two-layer design shown in Fig. 20. In both cases an air substrate ($\epsilon_{r1} = 1.0$) and a ceramic superstrate with$_{r2} = 55\% \pm 5\%$ was chosen (41). In both cases the layer thicknesses were chosen according to Eq. (1a) to produce a broadside beam at the operating frequency ($\theta_p = 0°$). Both E and H-plane patterns were measured for both antennas. In the H plane the full angular range of $-90° < \theta < 90°$ could be measured. In the E plane only the range $-45° < \theta < 80°$ was possible, due to a mechanical restriction in the measurements.

The first design, shown in Fig. 24, uses a circular radiating aperture and is designed to produce a broadside beam at a frequency of 62.2 GHz. The ceramic superstrate has a reported loss tangent of tan $\delta_{\epsilon i} = 0.002$ at a frequency of 6 GHz, but the loss tangent at the millimeter-wave operating frequency was unknown. The design equations (1a) with $l = 1$ and $m = 2$ determine the layer thicknesses as

$$d_1 = \frac{\lambda_{\epsilon 1}}{2} = 2.410\,\text{mm} \approx 2.4\,\text{mm} \qquad (68a)$$

$$d_2 = \frac{3\lambda_{\epsilon 2}}{4} = 0.487\,\text{mm} \approx 0.5\,\text{mm} \qquad (68b)$$

The values 2.4 mm and 0.5 mm were the actual thicknesses used in the measurements. The absorber layer above the superstrate has a thickness $d_3 = 2.5$ mm. The aperture diameter is 36 mm ($a \approx 3.7\lambda_0$). For this

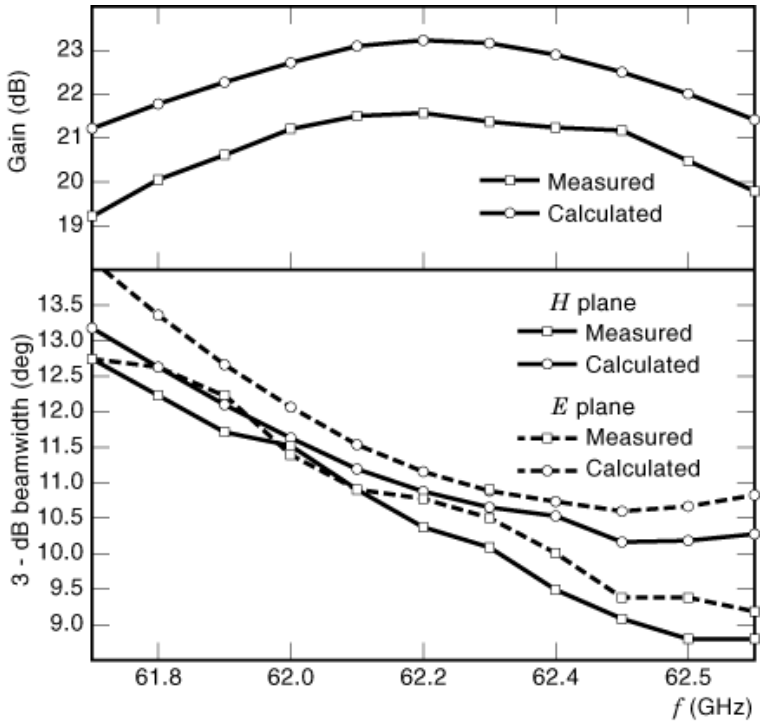

Fig. 25. Comparison between calculated (—○—) and measured (—□—) 3 dB beamwidth in the E and H planes, as well as calculated directivity (—○—) and measured gain (—□—) for the antenna structure shown in Fig. 24.

radius more than 95% of the dominant leaky-wave power will be radiated before reaching the absorber. To take the nonideal metal ground plane into account, a surface resistance $Z_s = 65$ mΩ was also considered in the calculation of the spectral-domain Green's function. The structure shown in Fig. 24 is excited using a waveguide with a slot at the aperture, which simulates an HMD_x source. (hence, the E-plane is $\theta = \pi/2$).The slot at the aperture is used for tuning purposes to improve the match seen by the waveguide feed. The slot dimensions are 2.37 mm by 1.88 mm.

The graphs in Fig. 25 show both theoretical and measured values for the 3-dB beamwidth and gain. As can be seen, the agreement for both beamwidth and gain is quite good. The deviation between simulated directivity and measured gain is probably caused in large part by the unknown loss tangent of the ceramic superstrate at 62.2 GHz.

Figure 26 shows the measured and calculated radiation patterns in both planes at 62.2 GHz. The cross-polarized component is 30 dB below the co-polarized component. As can be seen, this antenna has very good beam properties, with a low sidelobe level and a high polarization purity.

The second design illustrates that the 3 dB beam width can be lowered without increasing the superstrate permittivity or using a structure with more than two layers by using an array of sources. For example, more than one radiating slot can be placed in the ground plane, as illustrated in Fig. 27. In this case four resonant slots separated by a distance $\Delta d = 10$ mm are serial fed by a V-band waveguide operating at 61.5 GHz. The structure is covered by an absorber having an aperture that is approximately rectangular in shape. For this structure the radiation pattern was calculated by summing the patterns produced by the four separate slots, assuming a circular aperture of radius 18 mm for each slot. For this structure the ceramic superstrate thickness

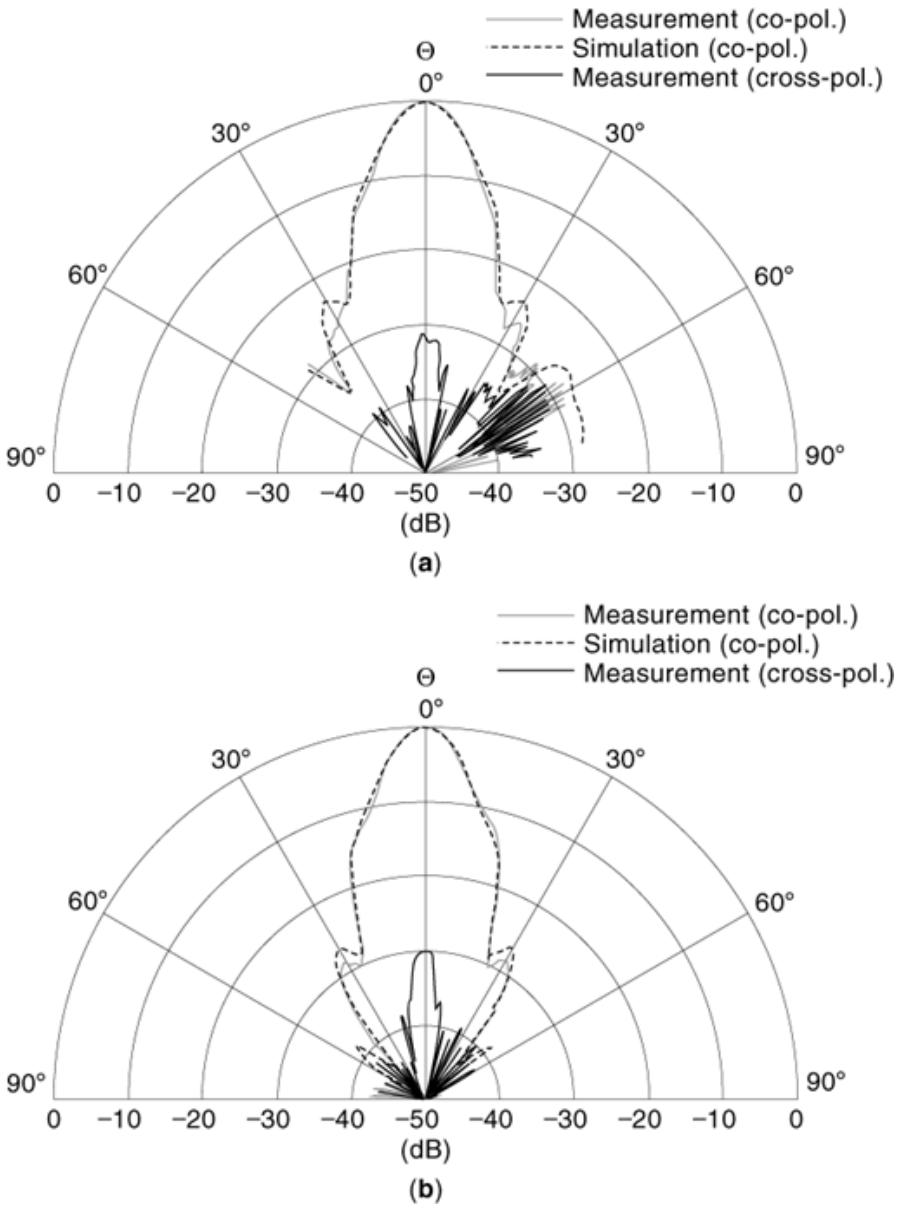

Fig. 26. Measured co-polarized (gray line), simulated co-polarized (—), and measured cross-polarized (—) radiation patterns in the (a) E plane ($\varphi = \pi/2$) and (b) H plane ($\varphi = 0$) at 62.2 GHz for the antenna structure shown in Fig. 24.

is again taken as 0.5 mm, whereas the thickness of the air substrate is adjusted slightly to a value of 2.45 mm to account for the slightly different frequency.

The slight asymmetry in the patterns shown in Fig. 28 is caused from a phase mismatch between the slots. But the use of multiple sources inside the leaky-wave guiding structure has demonstrated the possibility to achieve smaller 3 dB beam widths without resorting to multiple layers or very large permittivities.

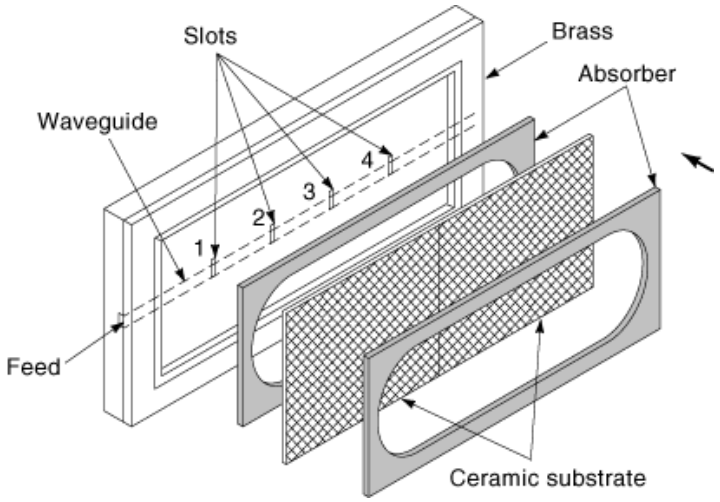

Fig. 27. Two-layer dielectric leaky-wave antenna structure excited by four resonant slots (1–4) of dimension 2.37 mm by 1.88 mm, fed by a V-band waveguide. The distance between the slots is $\Delta d = 10$ mm. The aperture size is 76 mm $\times$ 36 mm. $\varepsilon_{r1} = 1.0$, $d_1 = 2.45$ mm, $\varepsilon_{r2} = 55$, $d_2 = 0.5$ mm.

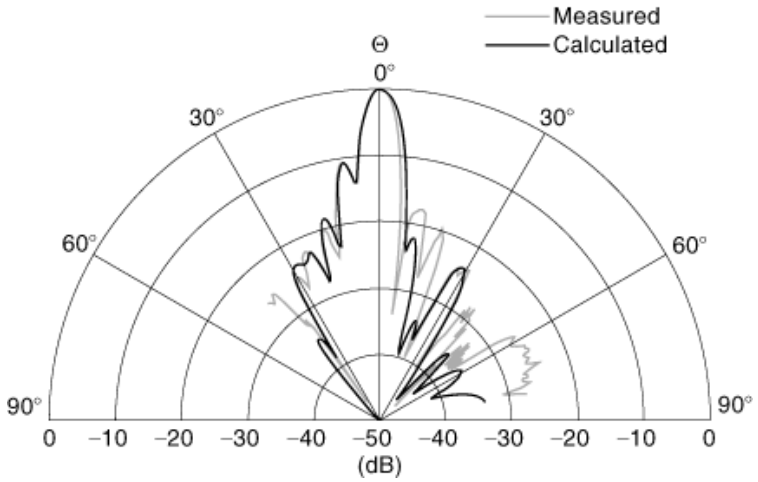

Fig. 28. Calculated co-polarized (—) and measured co-polarized (gray line) radiation patterns in the E plane (plane containing the array axis) at 61.5 GHz for the antenna structure shown in Fig. 27.

Alternative Feed and Aperture Configurations

The preceding section discussed in detail the analysis for a two-dimensional dielectric leaky-wave antenna structure consisting of a single dipole feed placed symmetrically at the center of a circular aperture. This type of antenna can produce either a broadside beam or a conical beam with a scan angle $\theta_p > 0$. For some applications, different feed arrangements may be desirable in order to realize different beam types. A few of these feeding arrangements are illustrated in this section. The first arrangement is one that produces a scanned unidirectional beam (pencil beam) instead of a conical beam.

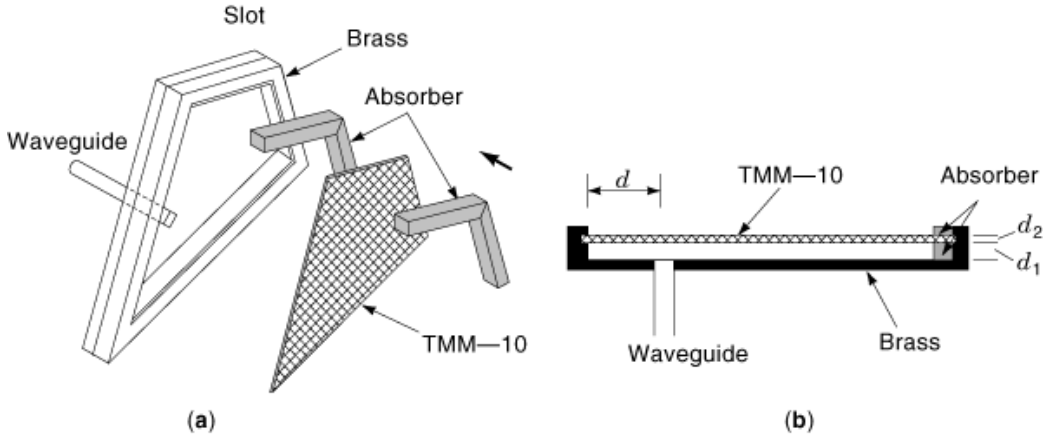

Fig. 29. Two-layer dielectric leaky-wave antenna that uses a 45° corner reflector to achieve a scanned unidirectional beam. (a) isometric view; (b) cross section.

To generate a unidirectional pencil beam, an aperture that supports a propagating leaky-wave field over a limited angular region (instead of a full 360° circular region) may be used (42). One such structure is shown in Fig. 29. This structure is a two-layer dielectric leaky-wave antenna with a wedge-shaped aperture formed by metallic 45° walls that form a corner reflector. The structure is terminated by a V-shaped absorber. For the particular structure shown, air is used as the substrate and a layer of TMM material (43) with $\varepsilon_{r2} = 9.2$ is used as the superstrate. The thicknesses $d_1 = 3.475$ mm and $d_2 = 1.25$ mm are used, which corresponds to $\theta_p = 45°$ at 61.0 GHz, using the design equations in Eq. 1a with $l = 1$ and $m = 2$. The feed is a magnetic dipole in the x direction placed along the bisecting line of the wedge at a distance d from the vertex. This feed is realized practically by using a rectangular V-band waveguide that has a slot in the aperture for matching purposes.

The calculation of the far-field pattern can be done by first calculating the tangential electric field on the aperture and then Fourier transforming this field, as discussed earlier. In order to calculate the aperture field, an approximate image representation of the source is used, as shown in Fig. 30 (The image model would be exact if the metallic walls of the corner reflector were infinitely tall.) The image model consists of the original dipole along with seven image dipoles, making up eight total magnetic dipoles arranged on the vertices of a regular octagon. The dipoles are 45° apart, and the distance from each dipole to the origin is d. Each dipole at $(x_i, y_i$ is resolved into x and y components as

$$M_{xi} = \delta(x - x_i)\delta(y - y_i)\cos\left((i-1)\frac{\pi}{4}\right) \qquad (69a)$$

$$M_{yi} = \delta(x - x_i)\delta(y - y_i)\sin\left((i-1)\frac{\pi}{4}\right) \qquad (69b)$$

with index i describing the position of the dipole. The distances ρ_i and angles φ_i measured from dipole i at (x_i, y_i) to the aperture point (x_p, y_p) are calculated as

$$\rho_i = \sqrt{(x_p - x_i)^2 + (y_p - y_i)^2} \qquad (70a)$$

$$\varphi_i = \arctan\frac{y_p - y_i}{x_p - x_i} \qquad (70b)$$

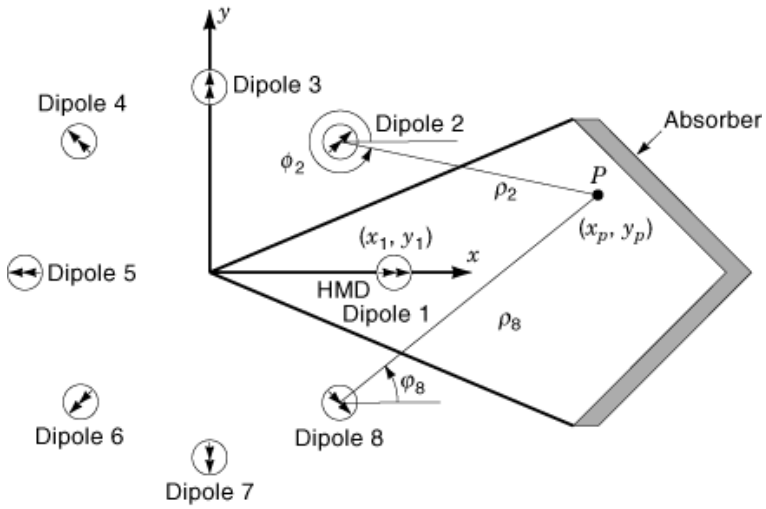

Fig. 30. Model of the corner-reflector leaky-wave antenna using image theory. The source excitation is the HMD_x dipole labeled 1.

The aperture field is then found by superposing the field of the eight dipole sources with the field from each source found as described in the preceding section.

To calculate the far-field pattern, the tangential electric aperture field is Fourier transformed, as discussed in the precceding section. Performing the integration in polar coordinates gives the result

$$E_\theta(r,\theta,\varphi) = 2R(r)\int_{-\pi/8}^{\pi/8}\int_0^{r(\varphi')}\Big[E_\rho(\rho',0)\cos(\varphi-\varphi') + E_\varphi(\rho',0)\,\sin(\varphi-\varphi')\Big]\times e^{jk_0\rho'\sin\theta\,\cos(\varphi-\varphi')}\rho'd\rho'd\varphi' \tag{71a}$$

$$E_\varphi(r,\theta,\varphi) = 2R(r)\cos\theta\int_{-\pi/8}^{\pi/8}\int_0^{r(\varphi')}\Big[-E_\rho(\rho',0)\sin(\varphi-\varphi') + E_\varphi(\rho',0)\cos(\varphi-\varphi')\Big]\times e^{jk_0\rho'\sin\theta\cos(\varphi-\varphi')}\rho'd\rho'd\varphi' \tag{71b}$$

where

$$R(r) = \frac{jk_0}{4\pi r}e^{-jk_0r} \tag{71c}$$

The double integration in these equations has to be performed numerically for each far-field observation coordinate (θ, φ).

To determine the optimum distance from the source to the vertex, an array factor based on the dominant leaky waves is used. For the proposed antenna configuration the optimum distance is found to be $d = 3.0$ mm.

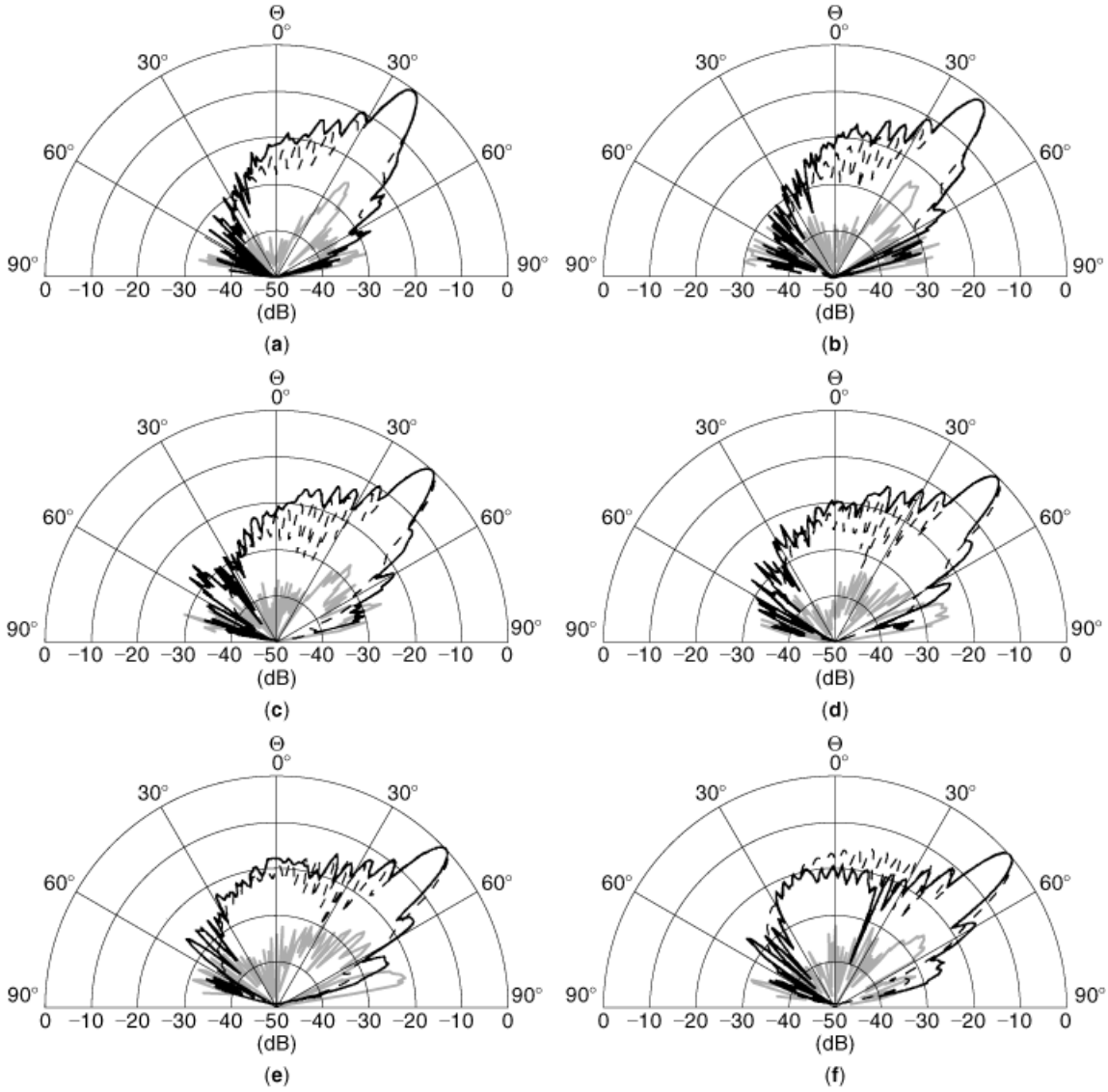

Fig. 31. Co-polarized measured field (—), calculated co-polarized field (—), and measured cross-polarized field (gray line) radiation patterns for the corner-reflector leaky-wave antenna at (a) $f = 55.0$ GHz, (b) $f = 57.0$ GHz, (c) $f = 59.0$ GHz, (d) $f = 61.0$ GHz, (e) $f = 63.0$ GHz, (f) $f = 65.0$ GHz. The parameters are $\varepsilon_{r1} = 1.0$, $d_1 = 3.475$ mm for the air layer and $\varepsilon_{r2} = 9.2$, $\tan\delta = 0.0017$, $d_2 = 1.25$ mm for the TMM-10 substrate. The distance from the dipole to the corner is $d = 3.0$ mm.

Measured and simulated radiation patterns in the H plane ($\varphi = 0$) for various frequencies are shown in Fig. 31. The co-polarized field in this plane is in the φ direction, with the cross-polarized field in the θ direction. The scanning nature of the beam with frequency is clearly seen in this figure.

In Fig. 32, a comparison between the theoretical and measured 3-dB beamwidth and gain for this corner-reflector leaky-wave antenna is shown. The H-plane beam width is much smaller than the E-plane beam width, since the leaky-mode field on the aperture is mainly propagating in the radial direction (which is the H-plane

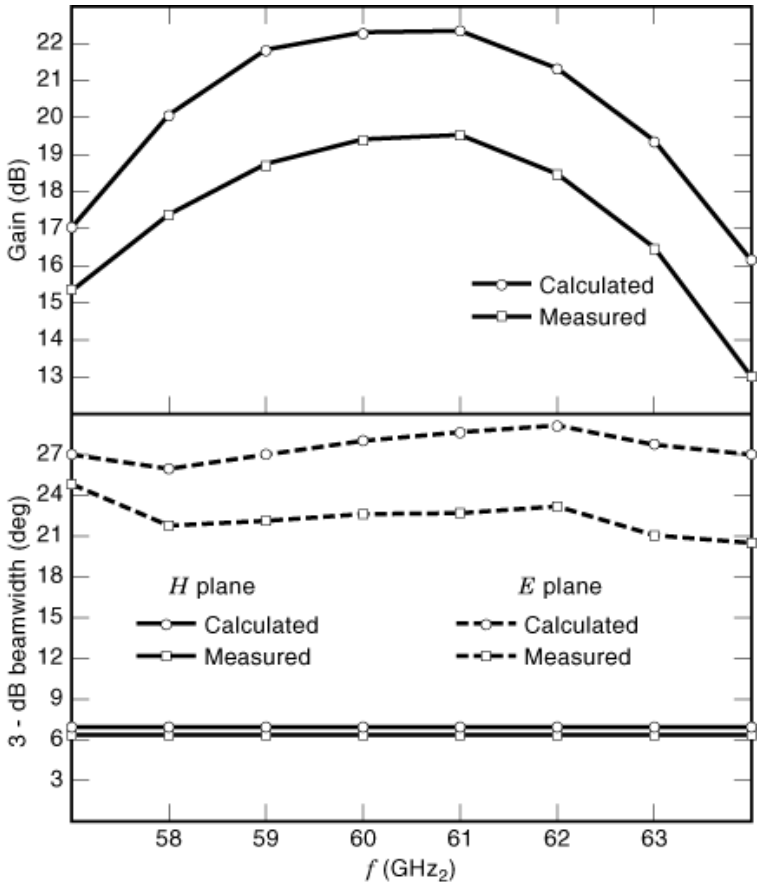

Fig. 32. Lower plot shows a comparison of simulated (—○—) and measured (—□—) 3-dB beam width in the H plane (lower set of curves) and the E plane (upper set of curves) versus frequency for the corner-reflector leaky-wave antenna. Upper plot compares the calculated directivity (—○—) and measured gain (—□—) versus frequency for the same antenna. The structural parameters are the same as in Fig. 31.

direction for the magnetic dipole feed). The agreement between the measured and calculated beamwidth is fairly good for the H plane, but worse for the E plane. This is probably due to the fact that an approximate boundary condition was used on the side walls of the corner reflector in the analysis. In particular, perfectly conducting side walls of infinite height were assumed in the calculation of the aperture field (so that image theory could be applied). However, due to the finite height of the side walls in the actual structure, a fringing of the aperture fields at the side walls is expected to occur. This would lead to an effective E-plane width of the structure at any given radius that is larger than the physical width, resulting in a narrower E-plane beaidth.

The fact that the measured gain is lower than the calculated directivity in Fig. 32 can probably be explained by a combination of two factors. First, it is possible that the actual loss tangent was higher than the assumed value of 0.0017. For example, calculations show that increasing the loss tangent to 0.01 would reduce the gain by about 1.1 dB. Secondly, tolerance errors in the thickness of the substrate would reduce the directivity (and hence gain). Calculations show that allowing the substrate thickness to vary in the range 3.458 mm $< d_1 <$ 3.492 mm results in a maximum drop in the directivity of approximately 3 dB.

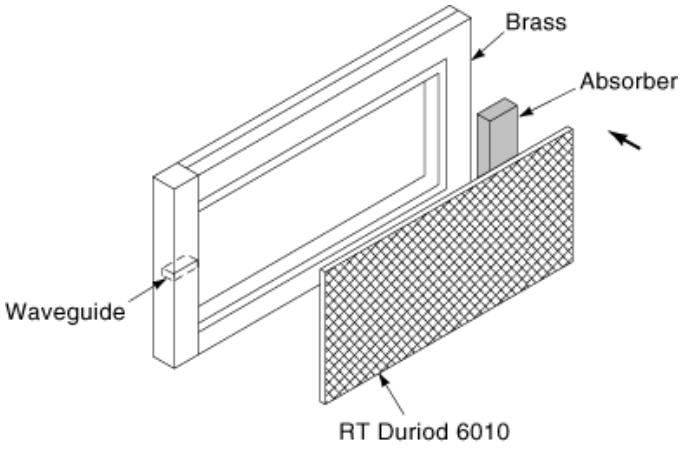

Fig. 33. Two-layer dielectric leaky-wave antenna structure with a rectangular aperture, fed by a waveguide along the center of one of the side walls. The two-layer structure has parameters $\varepsilon_{r1} = 1.0$, $d_1 = 3.475$ mm for the air layer, and $\varepsilon_{r2} = 10.8$, $\tan\delta = 0.0024$, $d_2 = 1.27$ mm for the RT-6010 duroid layer.

A second method for producing a unidirectional pencil beam is to use a rectangular aperture with an aperture field produced by a leaky-wave field propagating along the length of the aperture. Ideally, such a structure requires a line-source feed, so that a uniform excitation is produced across the width of the aperture. This type of leaky-wave antenna was originally investigated by Honey (44) at 12 GHz, using a dielectric grating leaky-wave antenna. Here, the two-layer dielectric leaky-wave antenna is used with a rectangular aperture, as shown in Fig. 33. Although a line source is the ideal feed for such an aperture, a single point-source type of feed can still be used, as shown in Fig. 33, where a waveguide feed is used. Such a feed will launch various Fourier-mode waves having different transverse wave numbers and hence different longitudinal propagation wave numbers. However, the use of a single feed has the advantage of simplicity.

Measurements are shown in Fig. 34 for various frequencies. In the calculations only the dominant TE_2 leaky mode was assumed, for simplicity. (The dominant TM_2 leaky mode is launched mainly in the E-plane direction, perpendicular to the long aperture dimension, making its effect less than that of the TE_2 leaky mode.) Also, for simplicity, an ideal absorber assumption was made in the analysis for all four walls (even though absorber was actually placed only along the end wall). That is, the aperture field was calculated by assuming an x-directed magnetic dipole in a structure with an infinite aperture, and then truncating the aperture field to the rectangular region. The calculated and measured co-polarized fields ($E\,\varphi$) and the measured cross-polarized field (E_θ in the $\varphi = 0$ plane are shown (where $\varphi = 0$ runs along the length of the aperture).

The H-plane beam characteristics, shown in this figure, are similar to those for the corner-reflector leaky-wave antenna shown in Fig. 31 except that the beam is broader and also the agreement between the calculated and measured patterns is not quite as good. The broader beam is due to the fact that a waveguide feed was used instead of a line-source type of feed (i.e., a point-source type of feed was used instead of a line-source type of feed). If the structure is fed using an E-plane horn, for example, to simulate a line-source feed, the beam can be narrowed significantly. The worse agreement between the calculated and measured results is probably due to the assumptions made in the analysis.

A dual-feed linearly polarized leaky-wave antenna is shown in Fig. 35, which incorporates two active silicon millimeter-wave integrated circuit (SIMMWIC) impatt oscillators. This antenna is fabricated completely using metallized plastic and is therefore very cost effective to produce. The oscillators radiate into a quadratic (square) waveguide, which supports both TE and TM polarizations. For hermetic purposes the whole structure is put onto a low-temperature cofire ceramic (*LTCC*) substrate. The absorber is made from a silicon mass filled

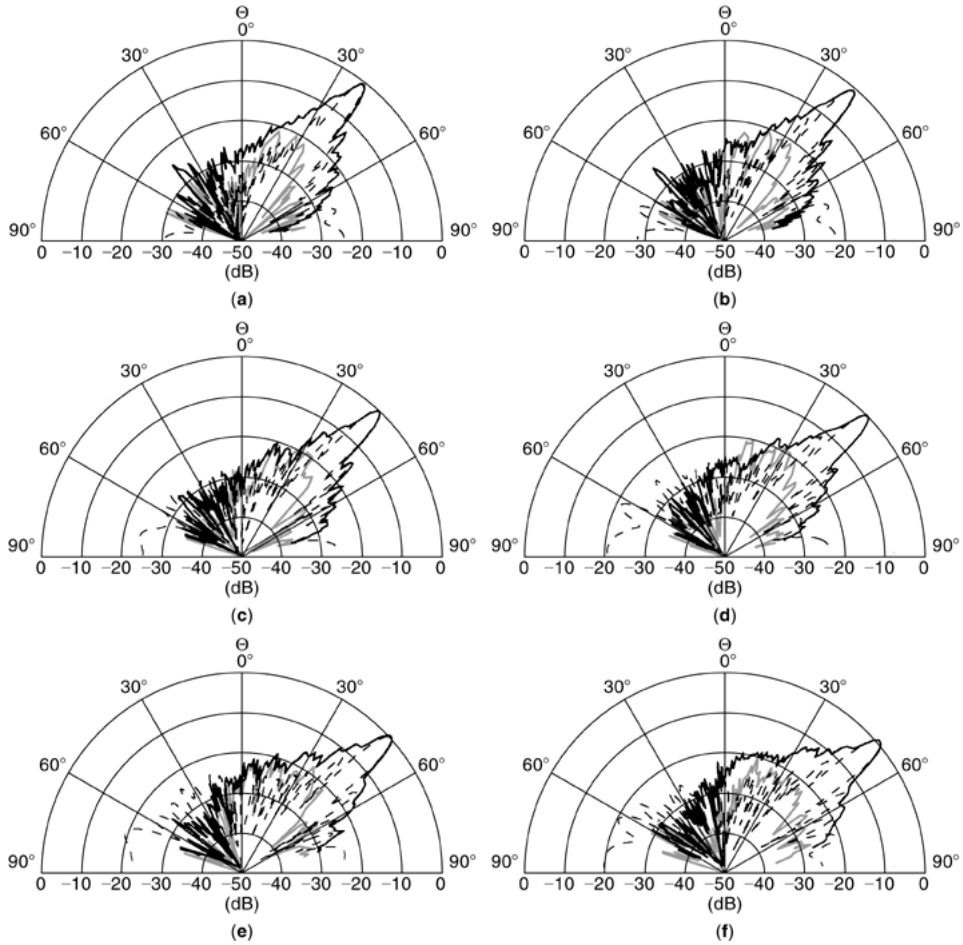

Fig. 34. Co-polarized measured field (—), calculated co-polarized field (—), and measured cross-polarized field (gray line) radiation patterns for the rectangular-aperture leaky-wave antenna shown in Fig. 33 at (a) $f = 55.0$ GHz, (b) $f = 57.0$ GHz, (c) $f = 59.0$ GHz, (d) $f = 61.0$ GHz, (e) $f = 63.0$ GHz, (f) $f = 65.0$ GHz. The parameters are $\varepsilon_{r1} = 1.0$, $d_1 = 3.475$ mm for the air layer and $\varepsilon_{r2} = 10.8$, $\tan\delta = 0.0024$, $d_2 = 1.27$ mm for the RT-6010 duroid layer.

with graphite (45). The cross-polarization level for this type of antenna is below 20 dB. This is sufficient for most applications.

Two last examples are presented in which multiple unidirectional beams are created. The first example is shown in Fig. 36, in which the principle structure from Fig. 33 has been complemented with an additional waveguide feed on the opposite side wall. The measured pattern in the H plane ($\varphi = 0$, with the x axis parallel to the long dimension of the aperture) clearly shows a dual beam.

This principle can be extended to multiple feeds. If four sources are used, placed on a square aperture, this configuration can be used as a position detector. The signals from the four receivers are exactly the same if the sensor is parallel to an arbitrary plane, because each receiver sees the same reflected signal. If the sensor is tipped, the signals are no longer the same, and one can calculate the angular deviation from a reference plane.

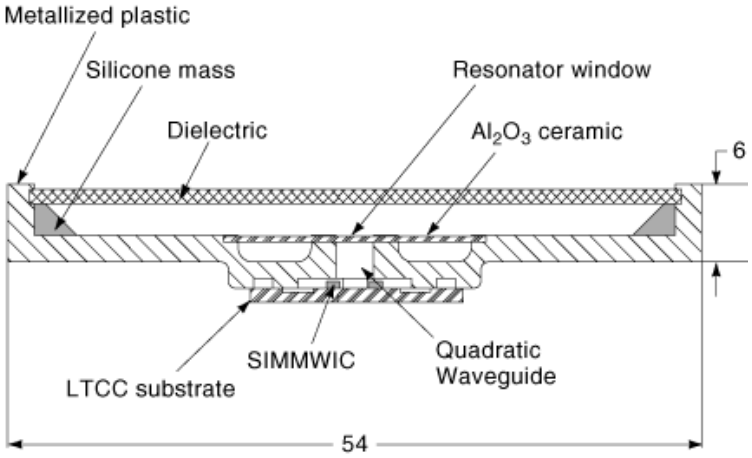

Fig. 35. Two-layer dielectric leaky-wave antenna structure with a double-linear polarized radiation beam, using two active impatt oscillator feeds.

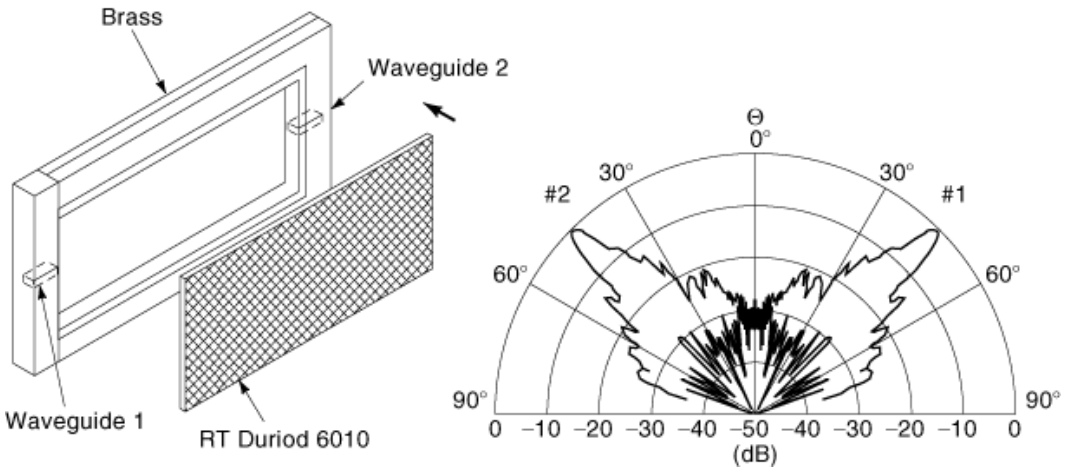

Fig. 36. Two-layer dielectric leaky-wave antenna structure with a rectangular aperture and two separate waveguide feeds at the opposite side walls, which allows for separate scanned unidirectional radiation beams. $f = 61.0$ GHz, $\theta_p = 45^\circ$, $\varepsilon_{r1} = 1.0$, $\varepsilon_{r2} = 10.8$, $d_1 = 3.475$ mm, $d_2 = 1.27$ mm. The measured H-plane co-polarized radiation field E_φ is shown, along with cross-polarized field E.

If eight feeds are placed equidistant around a circle, as shown in Fig. 37, digital beam forming can be applied to create a scanned beam with a scan angle of 360°.

A combination of the proposed antennas can be used in indoor communication environments. Due to their low profile, integration in walls, for example, is not too difficult. In one possible application, a low-gain omnidirectional scanned beam antenna could be used as a transmitter, while a high-gain broadside-beam antenna could be used as a receiver. The unidirectional antennas can also easily be used for monitoring purposes. The sensors could be located in a wall and used to illuminate a corridor, for example. Using the Doppler effect, moving objects can easily be detected. Active integrated antennas such as that shown in Fig. 35 are very cost-effective to produce, making it possible to build small inexpensive sensors for various applications

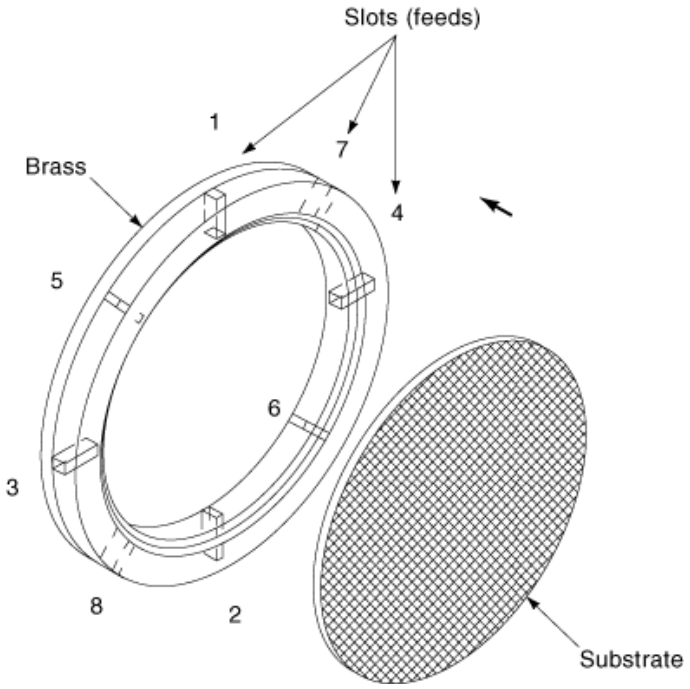

Fig. 37. Two-layer dielectric leaky-wave antenna having eight feeds arranged symmetrically on the perimeter of a circular aperture at $\varphi = 0^\circ$, 45°, 90°, 135°, 180°, 225°, 270°, and 315°.

in the automotive, radar, sensor, and communication areas. It is expected that such integrated antennas will find increasing applications in the future.

Conclusions

This article has reviewed a type of leaky-wave antenna known as the dielectric leaky-wave antenna. This type of antenna is simple, has a low profile at millimeter-wave frequencies, and can be used to create narrow-beam radiation patterns with a high efficiency. These antennas consist of one or more dielectric layers mounted over a ground plane, which creates a guiding structure for leaky waves. The thicknesses of the layers determines the propagation wave number of the leaky waves and hence the scan angle of the beam. Depending on the thicknesses of the layers, either broadside beams or scanned beams are possible. The leaky waves may be launched by using a simple source such as a waveguide feed. A review of the basic principles of operation, including a discussion of leaky waves, was given.

Several design variation were discussed. A one-dimensional form of the antenna was discussed in which a leaky wave propagates in one direction along the length of a narrow aperture. This type of antenna is suitable for creating beams that are narrow in one plane only (a fan beam). A two-dimensional form of the antenna was also discussed, in which the source launches a cylindrical set of leaky waves that propagate outward from the source on a two-dimensional aperture, which may be circular or rectangular in shape. This type of antenna can produce either a pencil beam at broadside or a conical beam at a scan angle $\theta_p > 0$. Several design variations were presented that have different aperture shapes or feed arrangements. These design variations allow for one or more scanned unidirectional pencil beams or dual-polarized beams.

The dielectric leaky-wave antennas discussed here can be used for automobile radar systems, mobile communication systems, sensors, and other applications at millimeter-wave frequencies. Due to their low profile these antennas can be integrated very easily with passive or active components. The fabrication process is also inexpensive, making mass production possible.

BIBLIOGRAPHY

1. N. B. Kramer, Must mm-waves wait again?, *Microw. J.*, **28**: 24–26, 1985.
2. J. Schwarz da Silva, B. Barani, B. Arroyo-Fernández European mobile communications on the move, *IEEE Commun. Mag.*, **34 (2)**: 60–69, 1996.
3. N. P. Morenc, MMICS for automotive radar applications, *1996 IEEE MTT-S Int. Microw. Symp. Digest*, 39–41, 1996.
4. B. Rembold, Communication systems at millimeter waves, *Proc. 22nd Eur. Microw. Conf.*, Helsinki, 1992, **Vol. 1**, pp. 53–72.
5. F. K. Schwering, Millimeter-wave antennas, *Proc. IEEE*, **80**: 92–102, 1992.
6. A. A. Oliner, *Scannable Millimeter Wave Arrays*, Weber Res. Inst., Polytechnic University, Technical Report No. Poly–WRI–1543–88, 1988, Vols. 1 and 2.
7. A. A. Oliner, Leakage from higher modes on microstrip line with application to antennas, *Radio Sci.*, **22**: 907–912, 1987.
8. M. Guglielmi A. A. Oliner, A practical theory for image guide leaky-wave antennas loaded by periodic metal strips, *Proc. 17th Eur. Microw. Conf.*, Rome, 1987, pp. 549–555.
9. F. Schwering S. T. Peng, Design of dielectric grating antennas for millimeter-wave application, *IEEE Trans. Microw. Theory Tech.*, **MTT-31**: 199–209, 1983.
10. P. J. Gibson, The Vivaldi aerial, *Proc. 9th Eur. Microw. Conf.*, 1979, pp. 101–105.
11. K. S. Yngvesson et al., Endfire tapered slot antennas on dielectric substrates, *IEEE Trans. Antennas Propag.*, **AP-33**: 1392–1400, 1985.
12. D. R. Jackson N. G. Alexopoulos, Gain enhancement methods for printed circuit antennas, *IEEE Trans. Antennas Propag.*, **AP-33**: 976–986, 1985.
13. H. Y. Yang N. G. Alexopoulos, Gain enhancement methods for printed circuit antennas through multiple superstrates, *IEEE Trans. Antennas Propag.*, **AP-35**: 860–863, 1987.
14. D. R. Jackson A. A. Oliner, A leaky-wave analysis of the high-gain printed antenna configuration, *IEEE Trans. Antennas Propag.*, **AP-36**: 905–910, 1988.
15. H. Ostner et al., Radiation from dielectric leaky-wave antennas with circular and rectangular apertures, *Electromagnetics*, **17 (5)**: 505–535, 1997.
16. D. R. Jackson, A. A. Oliner, A. Ip, Leaky-wave propagation and radiation for a narrow-beam multiple-layer dielectric structure, *IEEE Trans. Antennas Propag.*, **AP-41**: 344–348, 1993.
17. H. Ostner, J. Detlefsen, D. R. Jackson, Radiation from one-dimensional dielectric leaky-wave antennas, *IEEE Trans. Antennas Propag.*, **AP-43**: 331–339, 1995.
18. A. Ip D. R. Jackson, Radiation from cylindrical leaky waves, *IEEE Trans. Antennas Propag.*, **AP-38**: 482–488, 1990.
19. N. G. Alexopoulos, D. R. Jackson, P. B. Katehi, Criteria for nearly omnidirectional radiation patterns for printed antennas, *IEEE Trans. Antennas Propag.*, **AP-33**: 195–205, 1985.
20. J. A. Kong, *Electromagnetic Wave Theory*, New York: Wiley, 1990, p. 134.
21. T. Itoh, Spectral domain immitance approach for dispersion characteristics of generalized printed transmission lines, *IEEE Trans. Microw. Theory Tech.*, **MTT-28**: 733–736, 1980.
22. R. E. Collin, *Antennas and Radiowave Propagation*, New York: McGraw-Hill, 1985.
23. A. Sommerfeld, *Partielle Differentialgleichungen der Physik*, Frankfurt: Harri Deutsch, 1978, Bd. VI, Kap. 6.
24. V. W. Hansen, *Numerical Solution of Antennas in Layered Media*, New York: Wiley, 1989.
25. N. Marcuvitz, *Waveguide Handbook*, London: Peter Peregrinus, 1986, pp. 179–183.
26. R. E. Elliott, *An Introduction to Guided Waves and Microwave Circuits*, Englewood Cliffs, NJ: Prentice-Hall, 1993.
27. L. B. Felsen N. Marcuvitz, *Radiation and Scattering of Waves*, Englewood Cliffs, NJ: Prentice-Hall, 1973.

28. R. F. Harrington, *Time Harmonic Electromagnetic Fields*, New York: McGraw-Hill, 1961.
29. H. Shigesawa, M. Tsuji, A. A. Oliner, The nature of the spectral gap between bound and leaky solutions when loss is present in printed-circuit lines, *Radio Sci.*, **28 (6)**: 1235–1243, 1993.
30. R. Sorrentino, Transverse resonance method, in T. Itoh, ed., *Numerical Techniques for Microwave and Millimeter-Wave Passive Structures*, New York: Wiley, 1989, Chap. 11.
31. A. Ip, D. R. Jackson, A. A. Oliner, An improved calculation procedure for the radiation pattern of a cylindrical leaky-wave antenna of finite size, *IEEE Trans. Antennas Propag.*, **AP-40**: 19–23, 1992.
32. L. R. Rabiner, R. W. Schafer, C. M. Rader, The chirp z-transform algorithm and its application, *Bell Syst. Tech. J.*, **48**: 1249–1292, 1969.
33. L. R. Rabiner, R. W. Schafer, C. M. Rader The chirp z-transform algorithm, *IEEE Trans. Audio Electroacoust.*, **AU-17**: 86–92, 1969.
34. L. I. Bluestein, A linear filtering approach to the computation of the discrete Fourier transform, *1968 NEREM Rec.*, pp. 218–219.
35. A. V. Oppenheim R. W. Schafer, *Digital Signal Processing*, Englewood Cliffs, NJ: Prentice-Hall, 1975, pp. 321–326.
36. Y. L. Li, C. H. Liu, S. J. Franke, Adaptive evaluation of the Sommerfeld-type integral using the chirp z-transform, *IEEE Trans. Antennas Propag.*, **AP-39**: 1788–1791, 1991.
37. R. E. Collin, *Field Theory of Guided Waves*, New York: IEEE Press, 1991.
38. H. Ostner et al., A parallel-plate leaky-wave antenna using dielectric layers, PIERS, Nordwijk, Netherlands, 1994.
39. A. A. Oliner, *Scannable Millimeter Wave Arrays*, Weber Res. Inst., Polytechnic University, Technical Report No. Poly-WRI-1543-88, 1988, Vol. 1, pp. 71–73.
40. J. R. Mosig, Integral equation technique, in T. Itoh, ed., *Numerical Techniques for Microwave and Millimeter-Wave Passive Structures*, New York: Wiley, 1989, Chap. 3.
41. Stellar Industries, Data sheet MCT-55, 1993.
42. E. Schmidhammer, Analyse und Entwurf extrem flacher Leckwellenantennen für den Millimeterwellenbereich, Dissertation am Lehrstuhl für Hochfrequenztechnik, TU München, Germany, 1997.
43. Rogers Corporation, Data sheet TMM-10 substrate, 1995.
44. R. C. Honey, A flush-mounted leaky-wave antenna with predictable patterns, *IRE Trans. Antennas Propag.*, **AP-7**: 320–329, 1959.
45. General Electric Plastics GmbH, Data sheet C853 silicone mass, 1996.

EDGAR K. SCHMIDHAMMER
HELMUT W. OSTNER
JUERGEN B. DETLEFSEN
Technische Universität München
DAVID R. JACKSON
University of Houston